Experimental and Computational Simulation of a Model Ship in a Wind Tunnel

Ganesh Rajagopalan*
Iowa State University
Ames, IA

David Schaller†
Sukra Helitek, Inc.
Ames, IA

Alan J. Wadcock‡
Aerospace Computing, Inc.
Moffett Field, CA

Gloria K. Yamauchi§
NASA Ames Research Center
Moffett Field, CA

James T. Heineck¶
NASA Ames Research Center
Moffett Field, CA

Mark J. Silva‖
Naval Air Warfare Center
Patuxent River, MD

Abstract

Airwake measurements of an isolated 1/48th-scale amphibious assault ship were acquired in the U. S. Army 7- by 10-Foot Wind Tunnel at NASA Ames Research Center as part of a wind tunnel investigation of the shipboard aerodynamic interactions of a V-22 tiltrotor. Particle Image Velocimetry (PIV) was used to obtain 3-component velocity measurements in the cross-flow plane of the isolated ship wake at locations intersecting the rotor hub centers of an on-deck V-22. Data were acquired at several landing spots for various wind speeds and ship yaw angles. A subset of the measured velocity fields is compared with calculations from the unsteady, incompressible flow solver Rot3DC. The Rot3DC simulation closely modeled the experimental installation, including wind tunnel walls. Comparisons between measured and calculated velocities at the V-22 rotor plane are good, demonstrating the potential of Rot3DC in providing ship airwake information complementing the measured test matrix. Blockage issues were quantified by comparing Rot3DC calculations with and without wind tunnel walls. Blockage has only a small influence on the computed velocities at the rotor plane.

Introduction

In 1999 during shipboard compatibility trials, the V-22 aircraft experienced an uncommanded roll in response to another rotorcraft landing upwind of the V-22 on an L-class ship. The uncommanded roll of the V-22 was classified as a deficiency requiring correction prior to operational deployment. To resolve this V-22 Roll-On-Deck(ROD) problem, the V-22 Integrated Test Team (ITT) at NAVAIR launched a comprehensive multi-phase program consisting of mathematical-model development and validation in parallel with full-scale ground-based and shipboard down-wash surveys and interaction testing. The program led to the design, implementation and demonstration of a successful fix. One component of the multi-phase program included joint NAVAIR/Army/NASA wind tunnel investigations of the V-22 shipboard interactional aerodynamic phenomenon sponsored by the V-22 Program Office. The objectives of the V-22 ROD wind tunnel investigations were: 1) identify critical combinations of upwind aircraft position and wind-over-deck conditions based on measured roll moment response of an on-deck V-22, and 2) quantify the flowfield disturbance generated by the combined wake of the upwind rotorcraft and the ship for various rotorcraft operating upwind of an on-deck V-22 for use in an analytical study of the aircraft dynamic response. The wind tunnel tests

---

*Professor, Department of Aerospace Engineering and Engineering Mechanics, AIAA Associate Fellow
†Aerospace Engineer
‡Principal Scientist
§Aerospace Engineer
¶Photographic Technologist
‖Aerospace Engineer

were designed to acquire data for three primary installations: isolated ship, isolated aircraft, and ship plus on-deck V-22 with upwind rotorcraft. References [1] and [2] describe the first wind tunnel entry (completed in April 2002) of this joint investigation. Reference [3] describes measurements of the combined wake of the ship plus upwind tandem-rotor helicopter, in addition to limited isolated ship airwake measurements. The second wind tunnel entry, concluded in November 2003, investigated the combined wake of the ship and an upwind aircraft, with the upwind aircraft being either a tilt rotor or a single main-rotor helicopter. Both wind tunnel entries were conducted in the Army 7- by 10-Foot Wind Tunnel at NASA Ames Research Center using 1/48th-scale models.

The focus of this paper is the airwake of the isolated ship. Using Particle Image Velocimetry (PIV), 3-component velocity measurements were acquired at several landing spots along the ship deck for various wind speeds and ship yaw angles. The wind tunnel is an ideal environment for acquiring ship airwake data since the problems of variability in wind, sea state, and atmospheric conditions that plague full-scale sea trials do not exist. However, limited test time and geometric constraints of the model installation in the tunnel are obstacles to fully exploring the desired test conditions. A validated analysis that can fill in gaps of the experimental test matrix is therefore highly desirable. The U. S. Navy has performed several studies (Refs. [4], [5], [6], [7]) comparing the computed airwake of an LHA with full-scale data and with data from a 1/120th-scale wind tunnel model. The airwake was computed using COBALT, a Navier-Stokes solver using unstructured grids. References [4]-[7] describe how COBALT was used to examine airwake unsteadiness, effects of turbulence models on the computed results, Reynolds number independence, beam winds, and bow geometry. Results from these studies show that COBALT, while computationally expensive, is a promising tool for predicting ship airwakes.

The present investigation uses a subset of the PIV data from the 7- by 10-Foot Wind Tunnel test to assess the ability of a low-fidelity analysis tool, Rot3DC, to predict the velocity fields at specific locations along the isolated ship. Rot3DC, (Ref. [8]) is an unsteady, incompressible flow solver used for rotorcraft applications. For this investigation, Rot3DC uses laminar flow and a Cartesian grid system that simplifies the problem set-up by approximating solid surfaces as stair-stepped surfaces. This grid system results in compromised model geometry and a computationally economical solution. Despite the low-fidelity approach, Rot3DC has proved to be a useful and efficient tool for predicting trends of rotorcraft aeromechanic phenomena (Ref. [9]). The remainder of this paper describes the experimental set up, test conditions, Rot3DC analysis, and the computational simulation of the experimental set up. Comparisons between measured and computed velocity fields are presented at several landing spots along the ship deck. Blockage is addressed by comparing Rot3DC calculations with and without wind tunnel walls.

Model Installation

Isolated ship airwake data were acquired in the 7- by 10-Foot Wind Tunnel, a closed circuit wind tunnel operated by the U. S. Army Aeroflightdynamics Directorate at NASA Ames Research Center. The test section is 7-ft high and 15-ft long. The test section width is initially 10 ft but each sidewall diverges 1/4-degree to compensate for the effects of boundary layer growth. The tunnel has a maximum speed of approximately 350 ft/s. Four high-loss turbulence-reduction screens are installed in the return duct. The test section turntable is capable of yaw angles up to 360 degrees.

Figure 1 shows the ship installed in the 7- by 10-Foot Wind Tunnel. This ship was designed and built at NASA Ames Research Center and is a low-fidelity 1/48th-scale model of an LHA amphibious assault ship. Reference [10] provides details of the design methodology and construction of the model ship. Key ship dimensions are provided in Figure 2 and Table 1. Figure 1 shows the ship mounted 15 inches off-axis in the wind tunnel to accommodate upwind rotorcraft simulated flight patterns flown off the port side of the ship during other phases of the experiment. The ship was mounted on the turntable in order to provide model yaw.

The model-scale flight deck has several sets of markings known as "crow's foot" markings that duplicate full-scale markings at each landing spot. These markings provide visual cues to the pilot during shipboard rotorcraft approach, hover, descent and departure sequences. Each crow's foot marking, at full scale, consists

of 2 ft-wide white stripes that extend 10 to 30 ft laterally, forward, and diagonally inwards from the landing spot center. Equivalent line width at model scale is 0.5 inches. Each crow's foot is normally associated with a set of nose-wheel and landing gear wheel spots. At model scale, the nose-wheel markings are 1-inch downstream of each crow's foot. Numerous landing spot markings are visible in Figure 1. Figure 2 identifies individual landing spots on the port side of the ship.

Even at 1/48th-scale, the ship model is very large. From Table 1, overall deck width is 2.46 ft, length is 17.08 ft and height of deck above test section floor is 1.34 feet. Model blockage is non-negligible and is addressed later in the paper.

PIV Installation

Figure 3 is a schematic showing the relative placement of the laser light sheet (LLS), optics, PIV cameras, and ship. The LLS was positioned in the cross-flow plane at a fixed streamwise location in the tunnel. The ship was translated streamwise in order to document the flowfield at multiple deck locations. This eliminated the need for multiple camera calibrations. A very large measurement field was required to cover both ship air-wake and the wake from the rotorcraft flying approach patterns off the port side of the deck during other phases of the experiment. The PIV flow field was therefore centered in the test section despite the ship being mounted off-axis. The PIV flow field size was approximately 6-ft horizontal by 3-ft vertical.

A Spectra Physics PIV 400 dual-oscillator Nd:Yag laser with 350 mJ/pulse at 532 nm wavelength was used for the PIV measurements. Two high-resolution Kodak ES 4.0 2k x 2k digital cameras were used in order to provide the desired spatial resolution. These cameras were used in forward scatter, 30 degrees off-axis, in order to provide optimal particle visibility whilst maintaining acceptable perspective in the image. Each camera was equipped with a 50 mm f/1.4 Nikkor lens mounted on motorized rotation and translation stages to satisfy the Scheimpflug focusing condition.

A single Corona Integrated Technologies Vicount 5000 2.2 kW Series 180 mineral oil smoke generator was used to seed the flow. The nominal LLS thickness was 6 mm. The maximum out-of-plane particle displacement was kept small (less than 25% of the LLS thickness) in order to provide a strong correlation. In-plane particle displacements were kept below 4 pixels. Once satisfactory conditions were met, 100 frames of data were acquired for each test condition. The data were processed with a 24-pixel cross-correlation window. The corresponding spatial resolution of the measurements is 0.8-in horizontal and 0.4-in vertical (equivalent full-scale spatial resolutions of 3.4 ft and 1.7 ft, respectively).

Test Conditions

The motivation behind the PIV measurements was to understand the aerodynamic interactions influencing an on-deck V-22 due to the isolated ship airwake or due to the wake of an additional aircraft operating upwind. Although the on-deck V-22 was not present during the isolated ship airwake measurements, the PIV measurements were acquired in a vertical cross-flow plane intersecting the virtual V-22 rotor hub centers. Figure 4(a) shows a plan view of the model ship at zero degree yaw with the on-deck V-22 at Landing Spot 7 and a tandem-rotor helicopter being recovered at the upwind Landing Spot 6. The streamwise nose-wheel to rotor-hub distance for the V-22 is 18.125 ft at full-scale. At model scale this distance becomes 4.53 in. The LLS was therefore positioned 4.53 in downstream of the nose-wheel marker at each landing spot of interest in order to acquire downwash measurements at the rotor hub location of a virtual on-deck tilt-rotor. The full-scale V-22 rotor tip-path-plane is 20.83 ft above the ship deck. At model-scale this becomes 5.206 inches. The deck is nominally 16.13 in above the waterline at model scale. For efficiency, the position of the LLS in the tunnel was not changed as the ship was yawed. The result was a LLS that was no longer perpendicular to the longitudinal axis of the ship, and whose position moved slightly with respect to the desired location (the line joining the on-deck V-22 rotor hubs). This is illustrated in Figure 4(b).

Wind speeds for the isolated ship airwake measurements were selected to accommodate the reduced rotor tip speed of the model scale aircraft tested during a separate phase of the wind tunnel experiment. Ship-alone air-wake data were acquired with a clean deck, at multiple landing spots, for yaw angles between 0 and 15

degrees (positive yaw to starboard) and tunnel speeds from 5.6 to 33.8 ft/s (equivalent full-scale wind speeds of 10 to 60 knots) as indicated in Table 2. Complete documentation of the ship-alone air-wake measurements can be found in Ref. [2]. PIV measurements were not acquired at Landing Spots 5 and 6 due to blockage of the LLS by the ship superstructure. The current paper presents results for yaw angles of 0 and 15 degrees at a single wind speed of 22.5 ft/s.

Analysis Description

All computations were generated using Rot3DC, a general-purpose unsteady CFD solver for rotorcraft applications, Ref. [8]. This section summarizes the governing equations, numerical algorithm, and boundary conditions.

Governing Equations

The flow field of a laminar, unsteady, incompressible flow is governed by the mass and momentum equations. The mass equation is written as follows:

$$\nabla \bullet \left(\vec{V} \right) = 0 \tag{1}$$

The momentum equation in vector form can be written as:

$$\frac{\partial}{\partial t} \left(\rho u_i \right) + \nabla \bullet \left(\rho \vec{V} u_i - \mu \nabla u_i \right) = -\frac{\partial p}{\partial X_i} + V_i \tag{2}$$

for i = 1, 2, 3 where i denotes the specific direction.

In the above equations, ρ is the density, μ is the fluid viscosity, u_i is the ith component of the velocity vector, p is the pressure, and V_i includes the viscous terms which cannot be absorbed by the expression $\nabla \bullet (\mu \nabla u_i)$. An expression for V_i can be written in Cartesian tensor form as:

$$V_i = \frac{\partial}{\partial X_k} \left(\mu \frac{\partial u_k}{\partial X_i} \right) - \frac{2}{3} \frac{\partial}{\partial X_i} \left(\mu \frac{\partial u_k}{\partial X_k} \right) \tag{3}$$

for i = 1, 2, 3 where k is the repeated index summation, k = 1 to 3.

Numerical Algorithm

The numerical procedure to solve the fluid equations is based on Patankar's SIMPLER algorithm, Ref. [11], which seeks an iterative solution by solving the discretized conservation equations in a sequential line-by-line procedure. In this procedure, the primitive variables (static pressure and the components of velocity) are obtained directly by solving the mass and momentum equations. For a general variable Φ, representing any of u, v, w and p, the discretized equation at a grid point (i,j,k) is found to be:

$$\begin{aligned} a_{i,j,k} \Phi_{i,j,k} = {} & a_{i+1,j,k} \Phi_{i+1,j,k} + a_{i-1,j,k} \Phi_{i-1,j,k} \\ & + a_{i,j+1,k} \Phi_{i,j+1,k} + a_{i,j-1,k} \Phi_{i,j-1,k} \\ & + a_{i,j,k+1} \Phi_{i,j,k+1} + a_{i,j,k-1} \Phi_{i,j,k-1} \\ & + d_{i,j,k} \end{aligned} \tag{4}$$

where i, j, k are the grid indices, a's are the coefficients that link the neighboring Φ's to $\Phi_{i,j,k}$ and $d_{i,j,k}$ is the discretized form of the source term that consists of contributions from the specific governing differential equation being discretized.

4

Boundary Conditions

The boundary conditions at the edge of the global computational domain are easy to specify. At the inlet, free-stream conditions are imposed. If there is a ground plane or tunnel walls, the viscous no-slip boundary conditions are applied. All solid bodies are treated as blocked cells with no flow through them and viscous, no-slip conditions applied at the body surface. The outlet boundary, a plane parallel to the inlet boundary, is left for the numerical scheme to compute with mass conservation strictly enforced. If wind tunnel walls are not modeled, the freestream velocity is imposed at the side and upper boundaries.

Computational Simulation of Experiment

Rot3DC employed a single-block, 3D Cartesian grid system. The (X, Y, Z) coordinate system was fixed with respect to the wind tunnel. The origin of the coordinate system is shown in Figure 5. The X-direction (positive in the freestream direction) is parallel to the wind tunnel walls. Z is measured positive upwards from the water line (i.e., the wind tunnel floor). The computational domain (Figure 5) was divided into two main sections: the ship grid and the surrounding boundary grid. The boundary grid was modeled as a rectangular duct of constant cross-section. The boundary grid extends 12 ship-widths in front of and behind the ship. The ship grid box occupies a volume that contains the ship. The lateral position of the ship in the test section matches the experimental installation. Within the ship grid box, uniform grid spacing is used, with $\Delta X = 0.94$ in, $\Delta Y = 0.65$ in, and $\Delta Z = 0.44$ inch. Nonuniform grid spacing was used between the ship grid box and the boundary grid, with finer grid spacing (in X, Y, and Z) adjacent to the outer edges of the ship grid box and the boundary grid. Typical overall grid dimensions were 255x152x96.

For this paper, two ship orientations (yaw angles) were simulated with two different boundary conditions. The four cases are 1) yaw = 0 deg, with viscous boundary walls, 2) yaw = 0 deg, with free boundaries, 3) yaw = 15 deg, with viscous boundary walls, 4) yaw = 15 deg, with free boundaries. Cases 1 and 3 simulate the experimental set-up while Cases 2 and 4 were included to address the effect of blockage on the computed results. Figures 5 through 8 are plan views of the grid set-up for Cases 1-4, respectively. The ship grid remains unchanged for all four cases. For Cases 1 and 2, there are 46 grid points across the width and 219 grid points along the length of the ship deck. For Cases 3 and 4, the number of grid points defining the ship deck changes slightly as the ship is rotated within the ship grid box. All four cases use a viscous ground plane and were run with a steady and uniform inlet velocity of 22.5 ft/s (matching the experimental streamwise velocity).

The single-block Cartesian grid system prevents the grid from fitting precisely around the ship geometry except for the deck surface. For this study, this limitation is particularly pronounced for non-zero ship yaw angles (Cases 3 and 4), where the edges of the deck cut through the Cartesian grid at an angle creating a stair-stepped deck edge. The consequence of this non-body-fitted grid is that artificial roughness elements are introduced, particularly along the deck edges. These roughness elements lead to increased laminar diffusion. The introduction of a turbulence model will introduce additional diffusion which is not expected to improve the results and hence is not used. Initial research into grid refinement explored node clustering on the bow, port, and starboard edges of the deck. This investigation indicated that mesh refinement along the edges of the ship deck is critical to capture the generation of bow and edge vortices. Grid refinement inboard of the ship edge is also important to the downstream propagation of a vortex that is shed from the deck edge. The final grid chosen for the simulation was a compromise between computational efficiency and maintaining consistency between the rotated and non-rotated ship configuration.

The time step was chosen to be 0.005 seconds based on freestream velocity and the smallest ΔX grid spacing. Convergence was established by monitoring dilatation for each cell in the computational domain. Convergence was achieved when mass residual reached no more than 5.0E-5 slugs/s at any given cell within the computational domain. Each simulation was run for at least 4.0 seconds of real time. All solutions presented in this paper are time averaged over the last two seconds of computation. For a freestream velocity of 22.5 ft/s, two seconds of computation allows a released particle to travel more than 2.5 times the ship length. The total time of the simulation allows for at least one complete air exchange within the computational domain. The simulations were run on a PC using a linux OS with 2.0 GB of memory and a

2.4 GHz Intel XEON processor. Cases 1-4 each required approximately 168 hours of CPU time with each case requiring 5.5 GB of storage.

Results

Results from this investigation are presented in two sections. First, comparisons between Rot3DC calculations and measured velocity fields are presented for ship yaw angles of 0 and 15 deg at a wind speed of 22.5 ft/s. These calculations include the wind tunnel walls. The second section assesses the effect of blockage by comparing calculated results with and without wind tunnel walls for 0 and 15 deg yaw angles. Velocity fields are presented in the cross-flow plane. The streamwise (out of plane) velocity component, normalized with the free stream velocity Uinf, is presented in the form of iso-velocity colored contours. In-plane velocity components, scaled with the free stream velocity, are presented as velocity vectors. For the computed velocity plots, 25% of the in-plane velocity vectors are shown. For the PIV plots 11% of the velocity vectors are shown. Since the flowfield near the V-22 rotors is of particular interest for the V-22 ROD problem, the tip-path-plane of the rotors, the outline of the ship deck, and the outline of the superstructure are included in the appropriate figures to assist in interpreting the flowfield.

Comparison between calculations and measurements

Results for yaw = 0 deg are discussed first, followed by discussions for yaw = 15 degrees. As discussed earlier, PIV measurements were only acquired for Landing Spots 2, 4, 7 and 8.

Ship yaw = 0 deg.

Figure 9 provides a comparison between calculated and measured streamwise iso-velocity contours for a ship yaw angle of 0 degrees. Figure 9(a) shows Rot3DC calculations, walls included, for each of the portside landing spots. Figure 9(b) shows comparable PIV measurements. A more detailed comparison of the velocity fields (view looking upstream) is provided in Figure 10.

As shown in Figures 9 and 10, Landing Spots 2 and 4 lie upstream of the superstructure. The computed flowfield (Figures 9(a), 10(a)) is dominated by the wake from a laminar separation bubble at the bow of the ship. A laminar boundary layer separates from the bow of the ship and re-attaches on the deck as a laminar boundary layer. The separating laminar boundary layer of the model-scale ship, like the full-scale equivalent, is expected to undergo transition in the separated shear layer and re-attach as a turbulent boundary layer. Due to the increased entrainment associated with a turbulent shear layer, the separated shear layer can be expected to re-attach sooner, resulting in a thinner and shorter bubble followed by a thinner attached boundary layer. The calculated boundary layer at the center of the deck for Landing Spots 2 and 4 is much thicker than measured. Both calculations and measurements indicate the presence of counter-rotating deck vortices at each edge of the deck at Landing Spot 2, presumably originating from the gun cut-outs on either side of the deck at the bow of the ship. At Landing Spot 4 evidence of these deck vortices is no longer present in the calculated flowfield. In addition, the measurements indicate a more extensive upstream influence of the ship superstructure than the calculations at Landing Spot 4.

At Landing Spots 7 and 8, the flowfields are dominated by the superstructure wake. Reversed flow velocities in excess of 20% of Uinf are present at Landing Spot 7, but the velocity defect in the superstructure wake has recovered substantially by the time Landing Spot 8 is reached. At Landing Spot 7 the calculation shows uniform entrainment into the superstructure wake from all three sides, with no significant upwash in the plane of the rotors. This is confirmed by experiment. Experimental measurements in the top left of the flowfield for Landing Spots 7 and 8 show errors attributed to laser sheet curvature. The velocity defect measured in the superstructure wake is smaller than calculated. This is attributed to the increased turbulent diffusion present in the experiment compared to the laminar diffusion present in the calculations. Landing Spot 8 calculations show the relaxation of the superstructure wake to be slower than found experimentally, a result of the enhanced mixing in the turbulent wake of the experiment and a corresponding increased rate of wake recovery.

Figure 11 presents a comparison between Rot3DC calculations and measured upwash distributions across

the deck at the rotor tip-path-plane height of an on-deck V-22. Significant differences are encountered in the superstructure wake, as might be expected from the above discussion. At zero yaw the deck flow is fairly quiescent and both CFD and experiment indicate negligible upwash in the vicinity of the tilt-rotor tip-path-plane.

The growth of the deck boundary layer at yaw = 0 deg is examined in Figure 12. Zero yaw is chosen for this study because the influence of the deck vortex is minimal. Figure 12 presents computed and measured streamwise boundary layer profiles at each landing spot (that is, the streamwise rotor hub location for an on-deck tilt-rotor at each landing spot) plotted against height above deck (normalized by the tilt-rotor tip-path-plane height above deck). Calculations without wind tunnel walls are also presented in Figure 12. At Landing Spot 2, the Rot3DC calculations indicate a typical laminar boundary layer profile. PIV measurements indicate a very thin boundary layer at this location and do not capture the velocity profile. The actual deck boundary layer is assumed to be turbulent. Note that the laminar solution predicts a much thicker boundary layer than measured (for reasons explained in the discussion of Figure 10). At Landing Spot 4 the computed velocity profile still looks laminar. At Landing Spot 5, and downstream locations, the calculated boundary layer profile is now reminiscent of a turbulent boundary layer with a large wake component. Although Rot3DC is expected to provide a laminar boundary layer solution, the landing spots are located near the deck edge where the non-body-fitted Cartesian grid introduces artificial roughness leading to increased laminar diffusion. At Landing Spots 7 and 8 the computed and measured boundary layer profiles are similar. For the V-22 ROD problem, the deck boundary layer remains well below the height of the on-deck tilt-rotor tip-path-plane. The deck boundary layer is therefore expected to play little direct role in the ROD phenomenon.

In summary, for yaw = 0 deg, the deck boundary layer lies below the tip-path-plane of an on-deck tilt-rotor and has minimal impact at the rotor tip-path-plane. Calculated and measured results both show that upwash in the tip-path-plane of the rotors is negligible for Landing Spots 2, 4, 7, and 8.

Ship yaw = 15 deg.

Figure 13 provides a comparison between calculated and measured streamwise velocity contours for a ship yaw angle of 15 degrees. Figure 13(a) shows Rot3DC calculations, walls included, for each of the portside landing spots while Figure 13(b) shows comparable PIV measurements for Landing Spots 2, 4, 7, and 8. Compared with the calculated results for yaw = 0 deg shown in Figure 9(a), Figure 13(a) shows the superstructure wake is blown off the starboard side of the deck and plays no direct role with respect to landing spots on the port side of the ship. Also evident in Figure 13(a) and 13(b) is the appearance of a deck vortex originating at the gun cut-out (at the bow of the ship) on the port side of the deck. The deck vortex is seen to increase in size with distance down the deck. The laminar separation bubble encountered at the bow of the ship for zero yaw is no longer visible. Instead, a thickening of the deck boundary layer is evident along the port side of the deck, and this is seen to grow into what is referred to as the deck vortex.

Figure 14 provides side-by-side comparisons of the calculated and measured velocity fields (view looking upstream). As shown in Figure 13, the calculations indicate a greater streamwise velocity component in the vicinity of the ship than is measured experimentally (greater direct blockage effect). This discrepancy is a minor concern for assessing the ROD problem. At Landing Spots 2 and 4, the calculated and measured results both show a fairly thin deck vortex lying beneath the tip-path-plane of an on-deck tilt-rotor. At Landing Spot 2 the deck vortex is fairly weak and the induced velocity field mild, but at Landing Spot 4 significant upwash velocities are shown in the rotor tip-path-plane. Downstream of the superstructure the flowfield is extremely complex because of interaction between the deck vortex and the superstructure wake. At Landing Spot 7 calculations and measurements place the deck vortex above the right-rotor tip-path-plane. Notice the strong upwash through the left-rotor and mixed upwash/downwash through the right-rotor; this flowfield would induce a right-wing down rolling moment of an on-deck V-22. At Landing Spot 8, the deck vortex is located further to the right than at Landing Spot 7, so that the calculated and measured results indicate strong upwash through both left and right rotors of a tilt-rotor at this location. Note that the measurements indicate a thinner deck boundary layer and a smaller superstructure wake than computations. Neither of these discrepancies, however, preclude the success of predicting the flow in the vicinity of the rotor tip-path-plane.

Figure 15 presents a detailed comparison between Rot3DC calculations and measured upwash across the ship deck at the rotor tip-path-plane height of an on-deck V-22. At Landing Spot 2 there is excellent agreement between calculated and measured results. Landing Spot 4 shows slightly under-predicted deck vortex strength when compared with experiment. This under-prediction of the deck vortex strength is also visible at Landing Spots 7 and 8, but the agreement is generally satisfactory. In general, the location of the peaks and the valleys in the upwash distribution across the deck agree well, indicating that the deck vortex location is computed correctly. Asymmetry in upwash between the left and right rotors of the on-deck V-22 is expected to cause a significant rolling moment on the aircraft.

In summary, for yaw = 15 deg, the Rot3DC calculated flowfield in the vicinity of the V-22 rotor tip-path-plane compares well with experimental results. The deck vortex location is correctly predicted for Landing Spots 2 and 4. The primary features of the upwash velocity profiles at the V-22 tip-path-plane at Landing Spots 2, 4, 7, and 8 are captured. The deck boundary layer is well below the tip-path-plane of the V-22 rotors and should not directly contribute to the aerodynamics of ROD.

Blockage Assessment

Blockage is viewed as the sum of the model cross-sectional area normal to the free-stream plus displacement effects due to the boundary layer (or wake) on the model. Blockage is expected to have a direct effect on the streamwise component of velocity since model blockage results in an increase in the local bulk velocity through the wind tunnel. In the vicinity of the superstructure, the maximum blockage ratio (based on geometry) is 5.76% for the ship at a yaw angle of zero degrees. The corresponding value at 15 degrees yaw becomes 5.96%. In the following sections, Rot3DC calculations for Uinf = 22.5 ft/s are used to examine blockage effects by comparing calculations with and without wind tunnel walls. Results for yaw = 0 deg are discussed first, followed by discussions for yaw = 15 degrees.

Ship yaw = 0 deg.

Figure 16 shows an oblique view of the ship with the calculated airwake displayed at each port side landing spot along the deck. Figure 16(a), identical to Figure 9(a), shows Rot3DC calculations of the streamwise velocity including the effect of wind tunnel walls. Figure 16(b) shows the effect of removing the walls from the simulation. The location of the superstructure represents the position of maximum solid-body blockage. Blockage increases with downstream distance from the bow of the ship to the superstructure location. This monotonic increase in blockage is associated with a corresponding favorable streamwise pressure gradient. Apparently this favorable streamwise pressure gradient acting on the forward half of the ship, caused by the presence of wind tunnel walls, produces a smaller reversed flow bubble at the bow of the deck. The deck boundary layer computed with the presence of the walls, remains thinner at all downstream Landing Spot locations. Careful examination of Figure 16 confirms that the presence of wind tunnel walls produces a local increase in the streamwise velocity component above the deck and superstructure, a direct effect of model blockage, as expected.

Landing Spots 7 and 8 are the primary landing locations for the V-22, therefore, velocity fields for these two locations are examined next. Figures 17(a) and 17(b) present calculated velocity fields in the cross-flow plane at Landing Spot 7, with and without walls, respectively. The deck boundary layer is thinner, as observed previously, with walls present. There are no significant wall-effects at the tilt-rotor tip-path-plane location. Figures 18(a) and 18(b) present calculated velocity fields in the cross-flow plane at Landing Spot 8, with and without walls, respectively. The velocity defect in the superstructure wake has recovered substantially from Landing Spot 7 values with and without walls included in the simulation. Without walls (Figure 18(b)) the area of flow acceleration is to the port side of the ship, whereas with walls (Figure 18(a)) the whole vicinity of the ship shows streamwise acceleration.

Figure 19 shows the calculated upwash distribution across the ship deck at the tip-path-plane height of an on-deck tiltrotor for all landing spots. Each plot shows results with and without walls included in the simulation. Of particular interest are Figures 19(e) and 19(f) corresponding to Landing Spots 7 and 8, respectively. Only minor differences are seen between upwash profiles at the tip-path-plane location. The

largest differences are in the superstructure wake.

Ship yaw = 15 deg.

Figures 20(a) and 20(b) show the calculated airwake of the ship for yaw = 15 deg, with and without walls, respectively. Figure 20(a) is identical to Figure 13(a). Comparison between Figures 20(a) and 20(b) confirms an increase in the streamwise velocity component in the immediate vicinity of the ship associated with the presence of the wind tunnel walls. Overall flowfield features shown in Figures 20(a) and 20(b) are similar.

Figures 21(a) and 21(b) present the velocity field in the cross-flow plane at Landing Spot 7, with and without walls, respectively. The location of the deck vortex is unchanged between the two figures. The upper half of Figure 21(a) shows $U/U_{inf} > 1.1$ with walls, whereas Figure 21(b) shows $U/U_{inf} > 1.0$ for the almost identical region without walls. This direct effect of blockage was expected, although perhaps not at this magnitude. The superstructure wake is very similar between the two calculations. Figure 22 presents a similar comparison at Landing Spot 8. As observed at Landing Spot 7, the magnitude of the streamwise component of velocity in the vicinity of the ship is around 10% higher if wind tunnel walls are included in the calculation. In Figure 22(a), the center of the deck vortex is above and to the right of the right rotor of the on-deck tilt-rotor. As shown in Figure 22(b), the absence of walls does not significantly affect the vortex position.

Figure 23 presents a detailed comparison of the upwash distribution across the ship deck at the height of an on-deck tilt-rotor tip-path-plane for Landing Spots 2, 4, 5, 6, 7 and 8. Figures 23(a)-23(d), corresponding to Landing Spots 2-6, show negligible change in upwash across the deck due to the inclusion of wind tunnel walls. For Landing Spots 7 and 8 (Figures 23(e) and 23(f)), the largest differences caused by the inclusion of tunnel walls are in the superstructure wake. As for the zero yaw case, this area is on the starboard side of the deck, remote from the flowfield region of interest. Differences as high as 5% of Uinf are visible on the port side of the deck. In general, there is very little change in the upwash distribution across the deck at the rotor tip-path-plane that can be attributed to wall-effects.

Figure 24 provides further information on blockage effects present during the experiment. Figure 24 presents computed streamwise velocity through the test section close to the upper right corner of the duct, with and without walls, for zero and 15 deg yaw angles. At each yaw angle, the difference between the computations with and without walls represents the blockage effect at any streamwise station. For yaw = 15 deg, Figure 24 indicates that wall effects account for an approximate 10% increase in the streamwise velocity component above the superstructure (as previously discussed for Figures 21 and 22). In comparison, the maximum geometric blockage ratio of the ship at yaw = 15 deg is 5.96%. Clearly, simple estimates are inadequate to describe the blockage effects. A limited number of streamwise velocity measurements (acquired using a movable vane anemometer) are included for comparison with computations with walls. The upstream influence of the ship is larger than anticipated. The pressure signature of the ship is clearly visible in Figure 24 even 100 in ahead of the bow of the ship. The wind tunnel static ring is located only 52 in ahead of the bow of the ship. The left and right wall pressure taps of the static ring are ganged together in the wind tunnel to provide the reference static pressure that is used to infer freestream velocity. Examination of the CFD solutions imply that the experimental measurement of freestream velocity may be in error by as much as 0.5% due to upstream influence of the model. This error is smaller than the uncertainty in the PIV flowfield measurements. Therefore, the upstream influence of the ship is not considered significant for this investigation.

Conclusions

Airwake measurements of an isolated 1/48th-scale amphibious assault ship were acquired in the U. S. Army 7-by 10-Foot Wind Tunnel at NASA Ames Research Center as part of a wind tunnel investigation to investigate shipboard aerodynamic interactions of a V-22 tiltrotor. Particle Image Velocimetry (PIV) was used to obtain velocity measurements in the cross-flow plane of the isolated ship wake at locations intersecting the rotor hub centers of an on-deck V-22. Data were acquired at several landing spots for various wind speeds and ship yaw angles. Measured velocity fields for the isolated ship at Landing Spots 2, 4, 7, and 8 were compared with

calculations using the unsteady, incompressible flow solver Rot3DC. Comparisons of the flowfield near the V-22 rotors were of primary interest for this investigation. Blockage issues associated with the experiment were quantified by comparing Rot3DC calculations with and without walls. Results were presented for ship yaw angles of 0 and 15 deg and a freestream velocity of 22.5 ft/s. Major findings from the study are presented below.

1. Comparisons between Rot3DC calculations and measurements of the flowfield in the vicinity of the V-22 rotor tip-path-plane height (at Landing Spots 2, 4, 7, and 8) are satisfactory for ship yaw angles of 0 and 15 degrees. Computed deck vortex locations and upwash velocities at the rotor tip-path plane height compare well with measurements. Rot3DC is shown to be a useful tool for complementing the experimental test matrix.

2. For a ship yaw angle of 0 deg, the measured and calculated deck boundary layer lies below the tip-path-plane of an on-deck tilt-rotor and has minimal impact at the rotor tip-path-plane.

3. The flowfields calculated at Landing Spots 2, 4, 5, 6, 7, and 8 were examined with and without the inclusion of wind tunnel walls in the simulation. Absence of wind tunnel walls had minimal effect on the location of the deck vortex and the upwash velocities at the V-22 rotor tip-path plane height.

Acknowledgments

References

[1] Silva, M. J., Yamauchi, G. K., Wadcock, A. J., and Long, K. R., "Wind Tunnel Investigation of the Aerodynamic Interactions Between Helicopters and Tiltrotors in a Shipboard Environment," American Helicopter Society 4th Decennial Specialist's Conference on Aeromechanics, San Francisco, CA, January 2004.

[2] Yamauchi, G. K., Wadcock, A. J., Derby, M. R., Long, K. R., and Silva, M. J., "Results from the V-22/Ship/Helicopter Aerodynamic Interaction Phenomena (VSHAIP) Wind Tunnel Test," NASA TM to be published 2005.

[3] Wadcock, A. J., Yamauchi, G. K., Heineck, J. T., Silva, M. J., and Long, K. R., "PIV Measurements of the Wake of a Tandem-Rotor Helicopter in Proximity to a Ship," American Helicopter Society 4th Decennial Specialist's Conference on Aeromechanics, San Francisco, CA, January 2004.

[4] Polsky, S. and Bruner, C. W. S., "Time-Accurate Computational Simulation of an LHA Ship Airwake," AIAA-2000-4126, 18th AIAA Applied Aerodynamics Conference, Denver, CO, August 2000.

[5] Polsky, S., "A Computational Study of Unsteady Ship Airwake," AIAA-2002-1022, 40th AIAA Aerospace Sciences Meeting, Reno, NV, January 2002.

[6] Polsky, S., "CFD Prediction of Airwake Flowfields for Ships Experiencing Beam Winds," AIAA-2003-3657, 21st AIAA Applied Aerodynamics Conference, Orlando, FL, June 2003.

[7] Czerwiec, R. M. and Polsky, S., "LHA Airwake Wind Tunnel and CFD Comparison with and without Bow Flap," AIAA-2004-4832, 22nd AIAA Applied Aerodynamics Conference, Providence, RI, August 2004.

[8] Rajagopalan, R. G., "A Procedure for Rotor Flowfield and Interference: A Perspective," AIAA-2000-0116, 38th AIAA Aerospace Sciences Meeting, Reno, NV, January 2000.

[9] Potsdam, M. A., Schaller, D. F., Rajagopalan, R. G., and Silva, M. J., "Tilt Rotor Aeromechanics Phenomena in Low Speed Flight," American Helicopter Society 4th Decennial Specialist's Conference on Aeromechanics, San Francisco, CA, January 2004.

[10] Derby, M. R. and Yamauchi, G. K., "Design of 1/48th - Scale Models for Ship-Rotorcraft Interaction Studies," AIAA-2003-3952, 21st AIAA Applied Aerodynamics Conference, Orlando, FL, June 2003.

[11] Patankar, S. V., *Numerical Heat Transfer and Fluid Flow*, Hemisphere Publishing Corporation, New York, 1980.

Table 1. Ship Geometry

	Full Scale LHA	1/48th-scale model
Flight deck length	820 ft	205.0 in
Flight deck width	118.1 ft	29.53 in
Nominal deck height above waterline	64.5 ft	16.13 in

Port Landing Spot	Distance of nose-wheel mark from bow of ship	
2	127.5 ft	31.88 in
4	232.5 ft	58.13 in
5	337.5 ft	84.38 in
6	442.5 ft	110.63 in
7	547.5 ft	136.88 in
8	697.5 ft	174.38 in

Table 2. Isolated Ship Airwake Test Conditions

LLS Location[a]	V (ft/s)	Yaw (deg)
2	5.63	0,10
	11.25	0,5,10,15
	16.88	0,10
	22.5	0,5,10,15
4	5.63	0,10
	11.25	0,5,10.15
	16.88	0,10
	22.5	0,5,10,15
7	5.63	0,10
	11.25	0,5,10,15
	16.88	0,10
	22.5	0,5,10,15
	28.13	0
	33.76	0
8	5.63	0,10
	11.25	0,5,10,15
	16.88	0,10
	22.5	0,5,10,15
	28.13	0
	33.76	0

[a]LLS sheet was located 4.53 in downstream of the indicated landing spot nose-wheel mark.

Figure 1. 1/48th-scale amphibious assault ship installed in 7- by 10-Foot Wind Tunnel at NASA Ames.
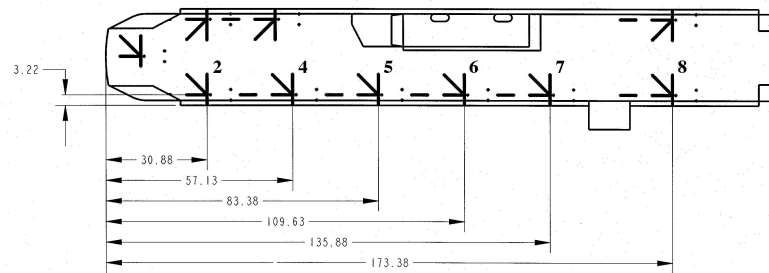
Figure 2. Location of model LHA landing spots (inches).

Sheet forming
optics

Mirrors

Laser

Laser sheet

Cameras
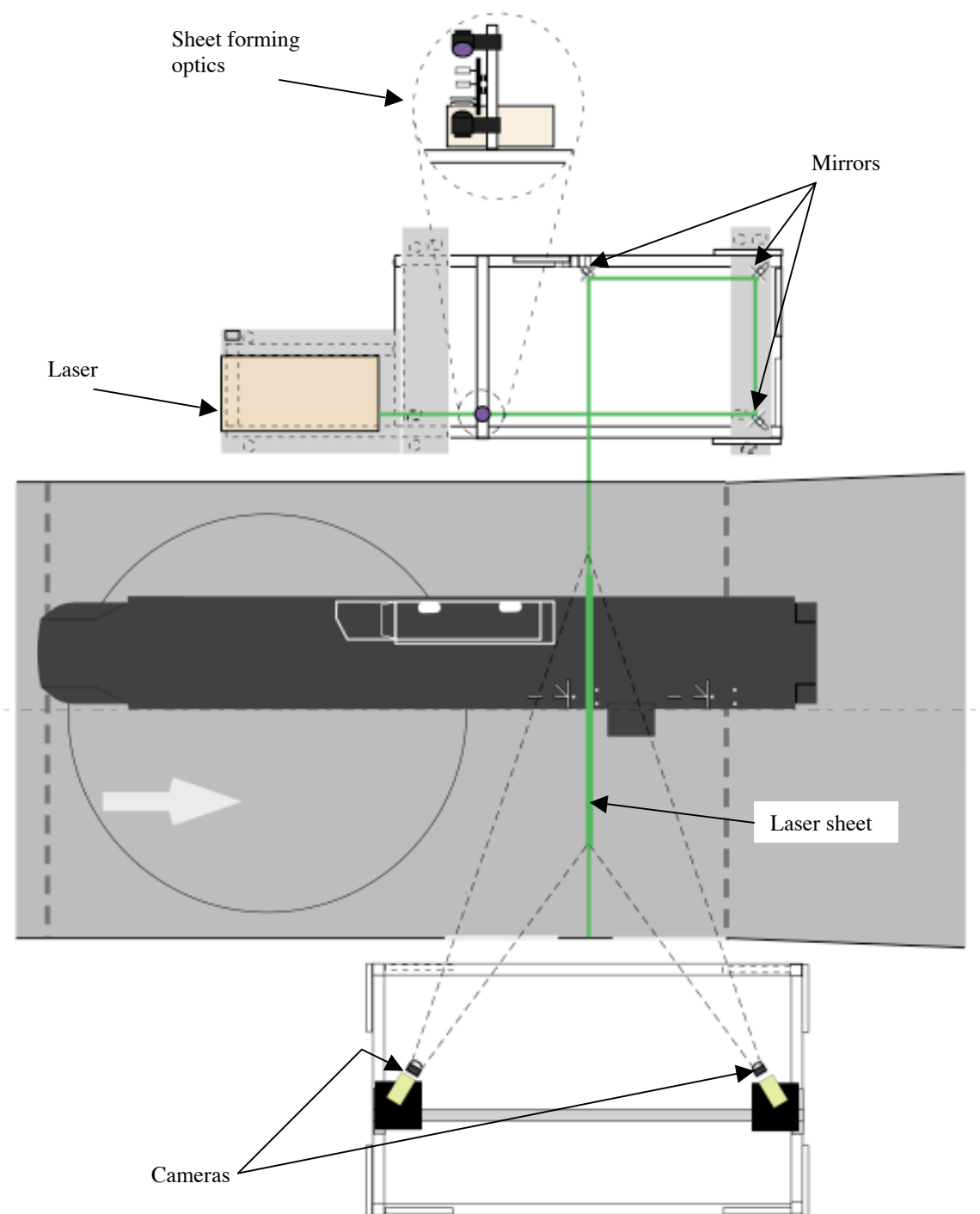
Figure 3. Plan view of PIV set-up in the 7- by 10-Foot Wind Tunnel.
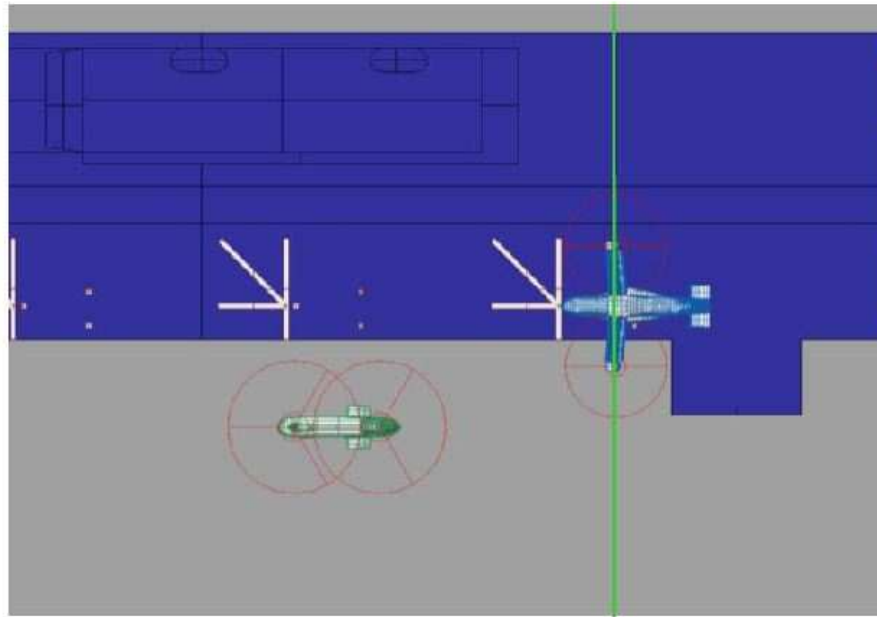
(a) On-deck V-22 at Landing Spot 7. Ship and upwind model yaw = 0 deg.
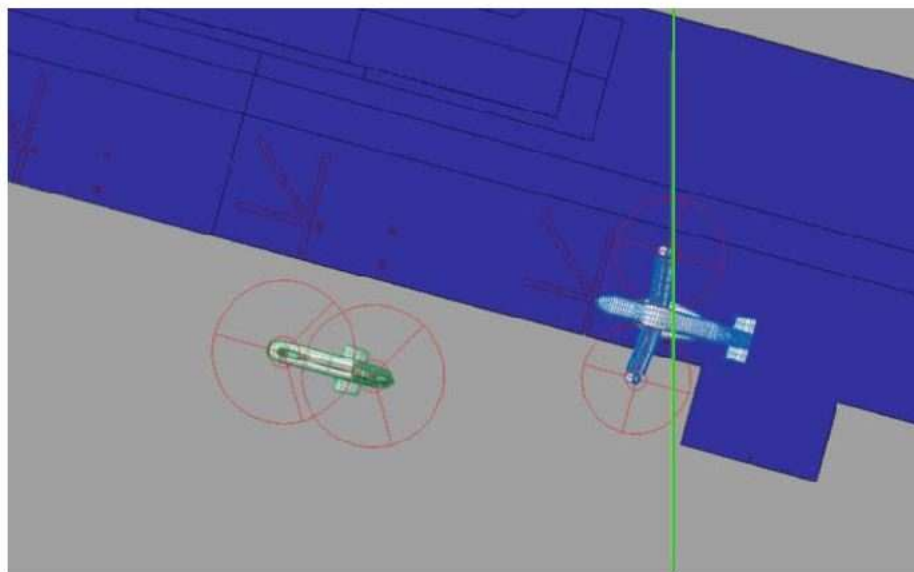
(b) On-deck V-22 at Landing Spot 7. Ship and upwind model yaw = 15 deg.

Figure 4. Location of PIV measurement-plane in wind tunnel.

SHIP WITH VISCOUS BOUNDARY WALLS (Yaw = 0 deg)
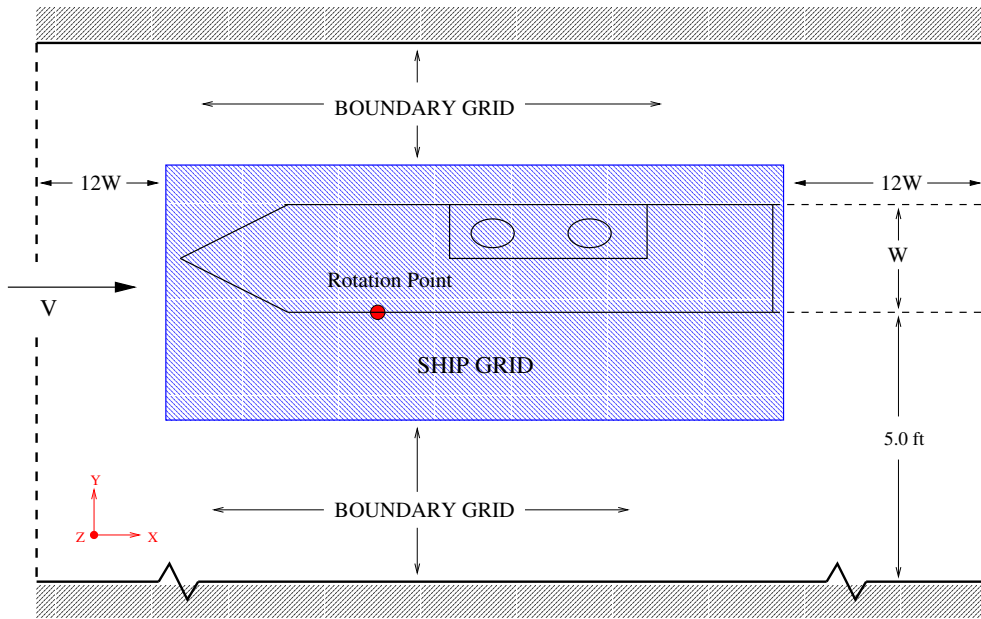
Figure 5. Plan view of computational grid set up: ship with viscous boundary walls for yaw = 0 deg.

SHIP WITHOUT VISCOUS BOUNDARY WALLS (Yaw = 0 deg)
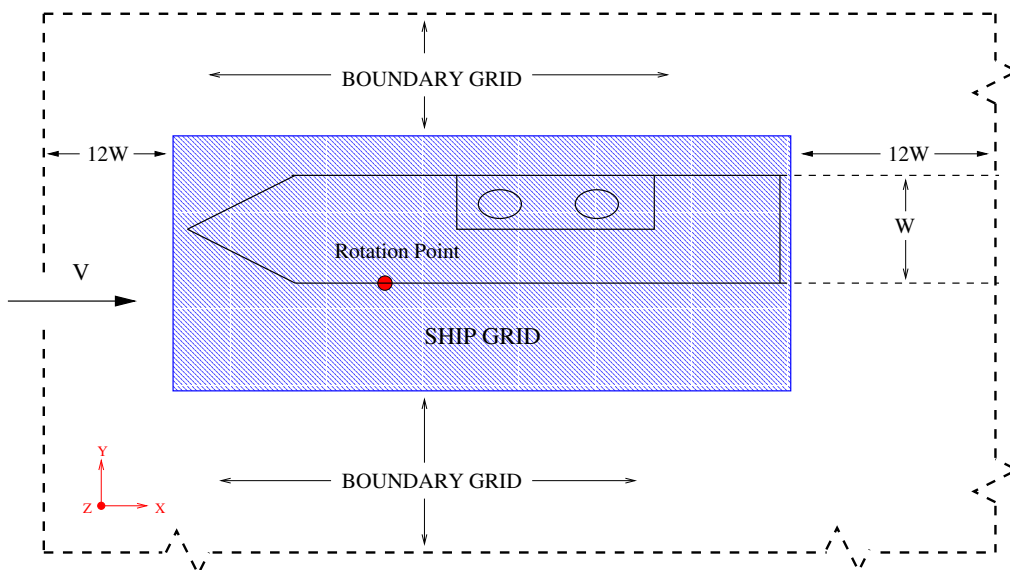
Figure 6. Plan view of computational grid set up: ship without walls for yaw = 0 deg.

SHIP WITH VISCOUS BOUNDARY WALLS (Yaw = 15 deg)
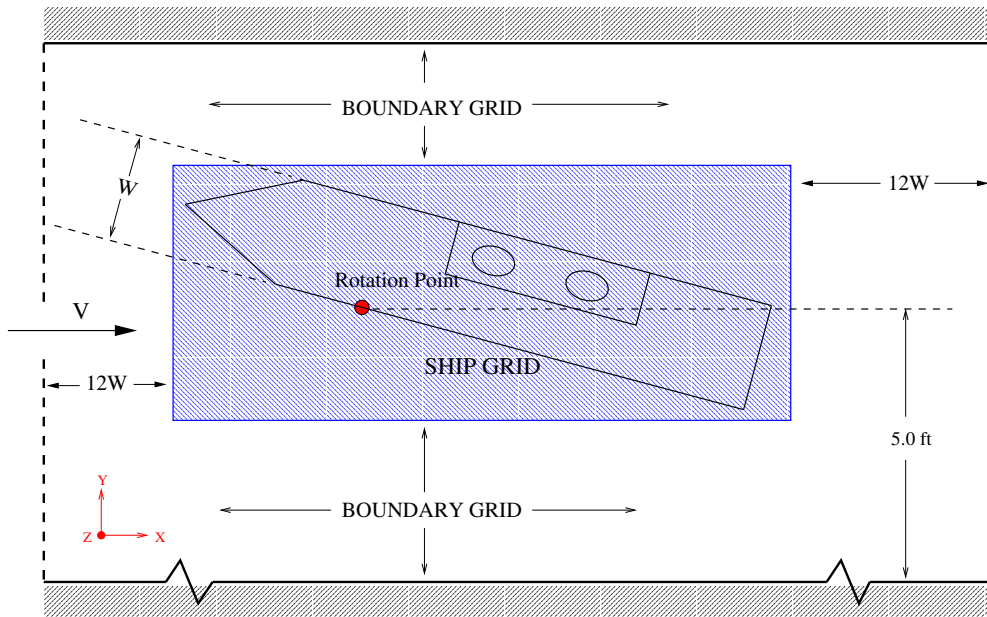
Figure 7. Plan view of computational grid set up: ship with viscous boundary walls for yaw = 15 deg.

SHIP WITHOUT VISCOUS BOUNDARY WALLS (Yaw = 15 deg)
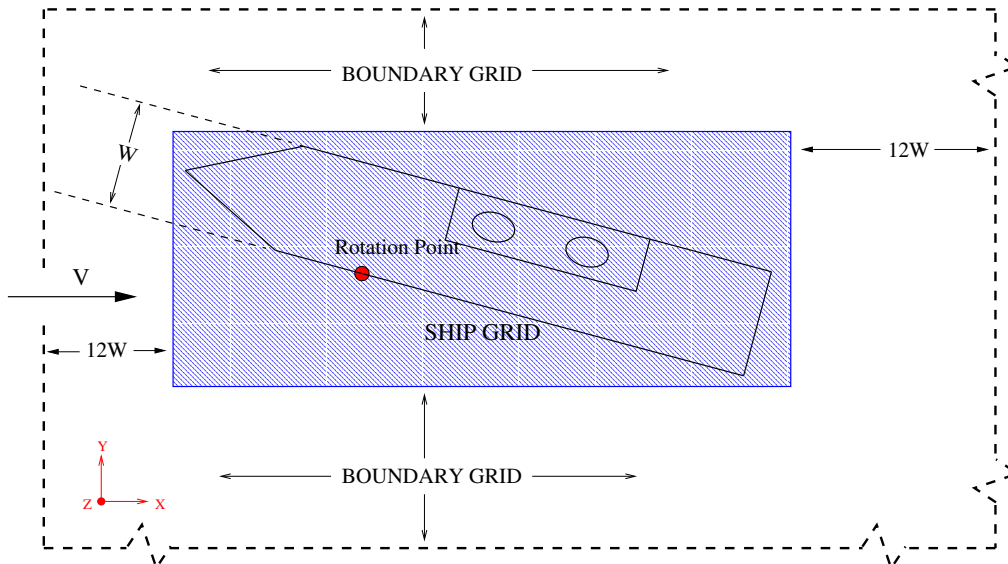
Figure 8. Plan view of computational grid set up: ship without walls for yaw = 15 deg.
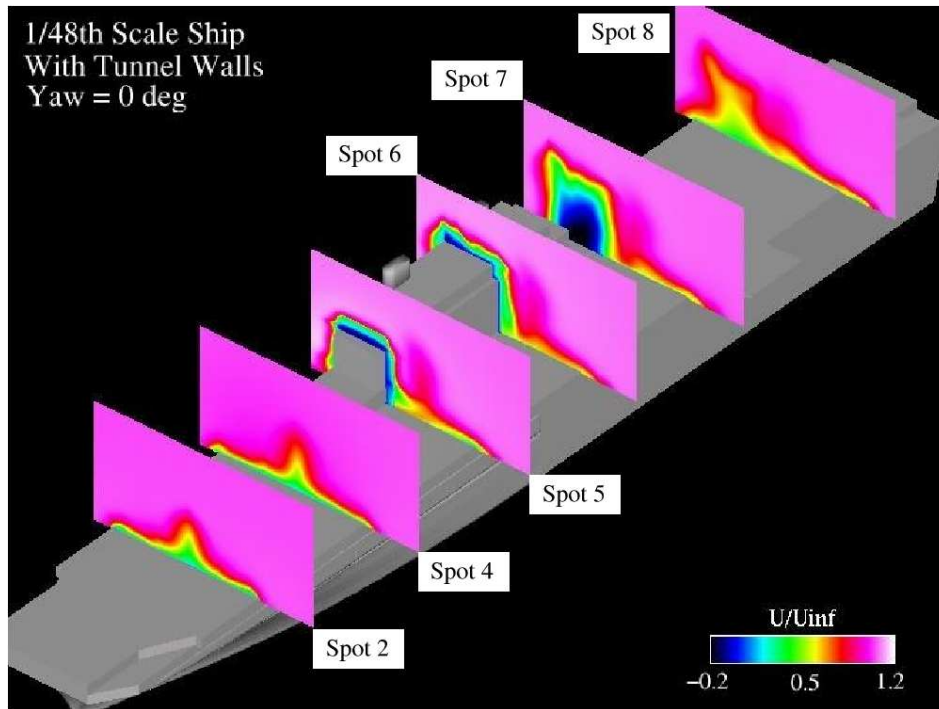
(a) Calculation (with walls)
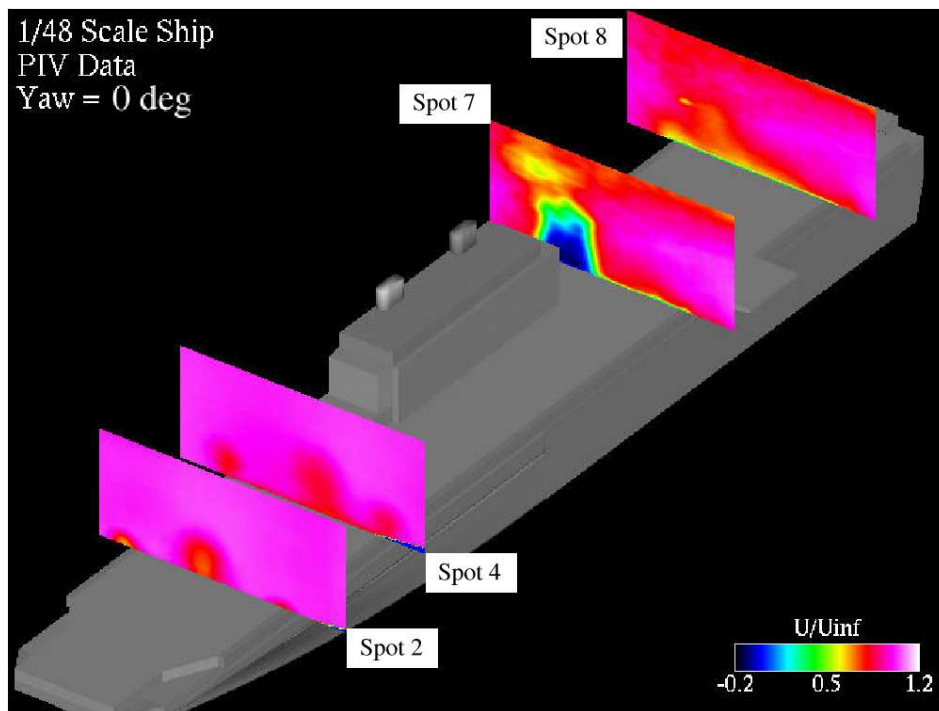
(b) PIV measurements

Figure 9. Comparison between calculated and measured ship airwake for yaw = 0 deg. Uinf = 22.5 ft/s.

18
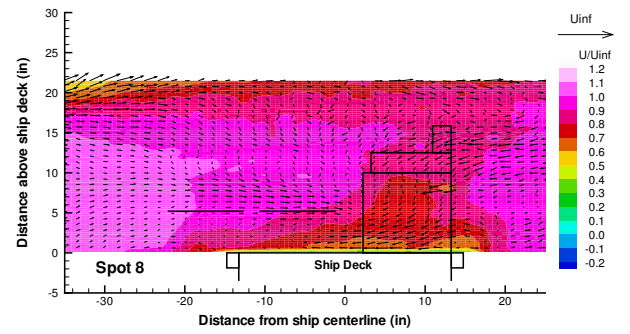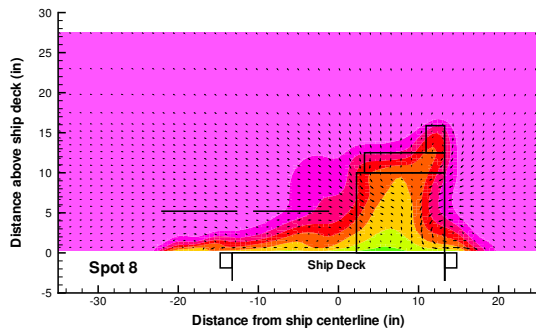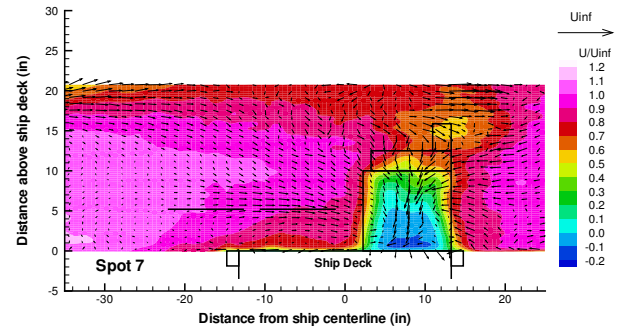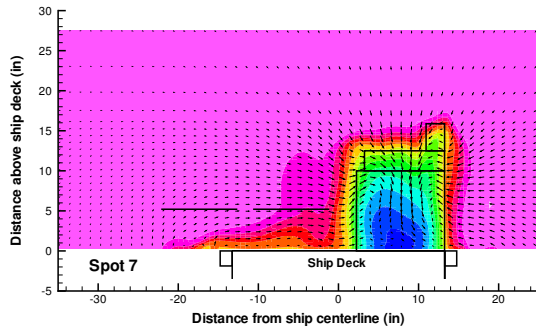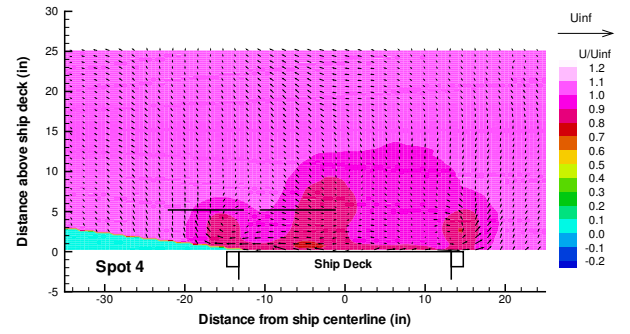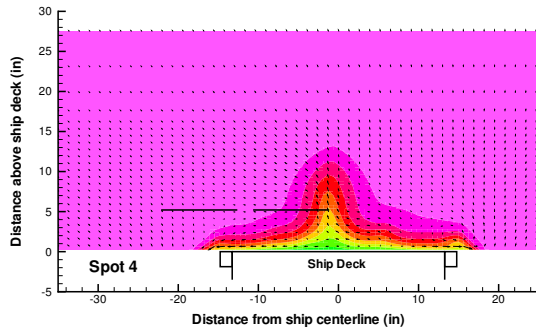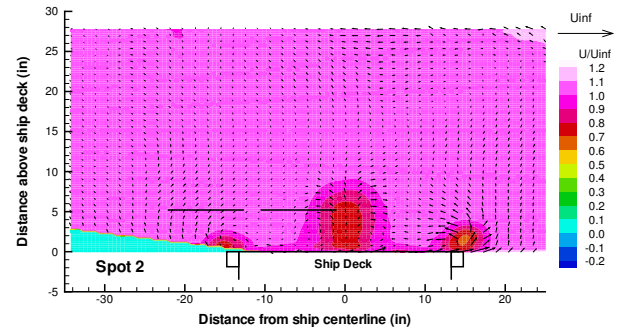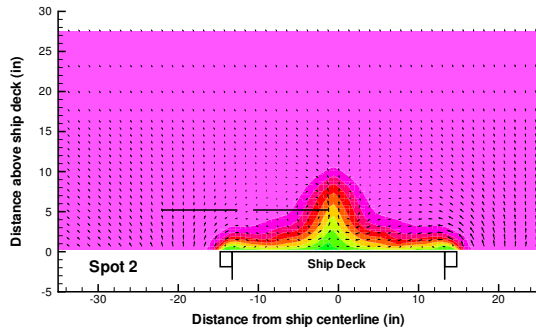
(a) Calculation (with walls)

(b) PIV measurements

Figure 10. Comparison between calculated and measured velocity fields for Landing Spots 2, 4, 7 and 8. Ship yaw = 0 deg. Uinf = 22.5 ft/s. View looking upstream.

19
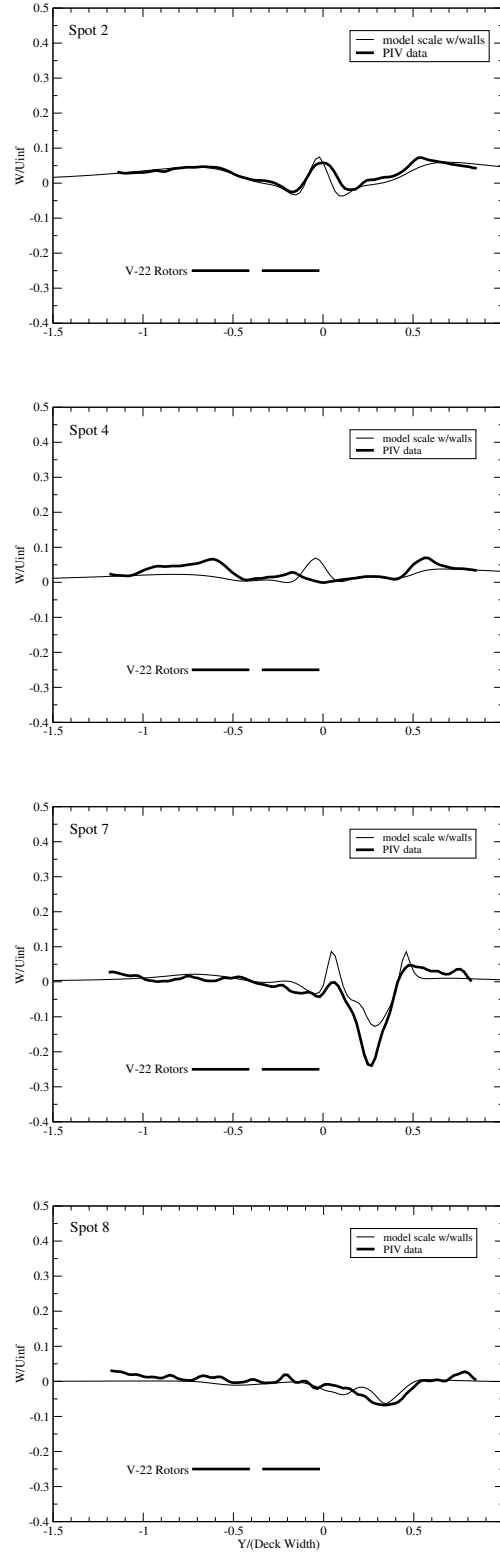
Figure 11. Comparison between calculated and measured vertical velocity across the ship deck at Landing Spots 2, 4, 7 and 8. Ship yaw = 0 deg. Uinf = 22.5 ft/s.

20
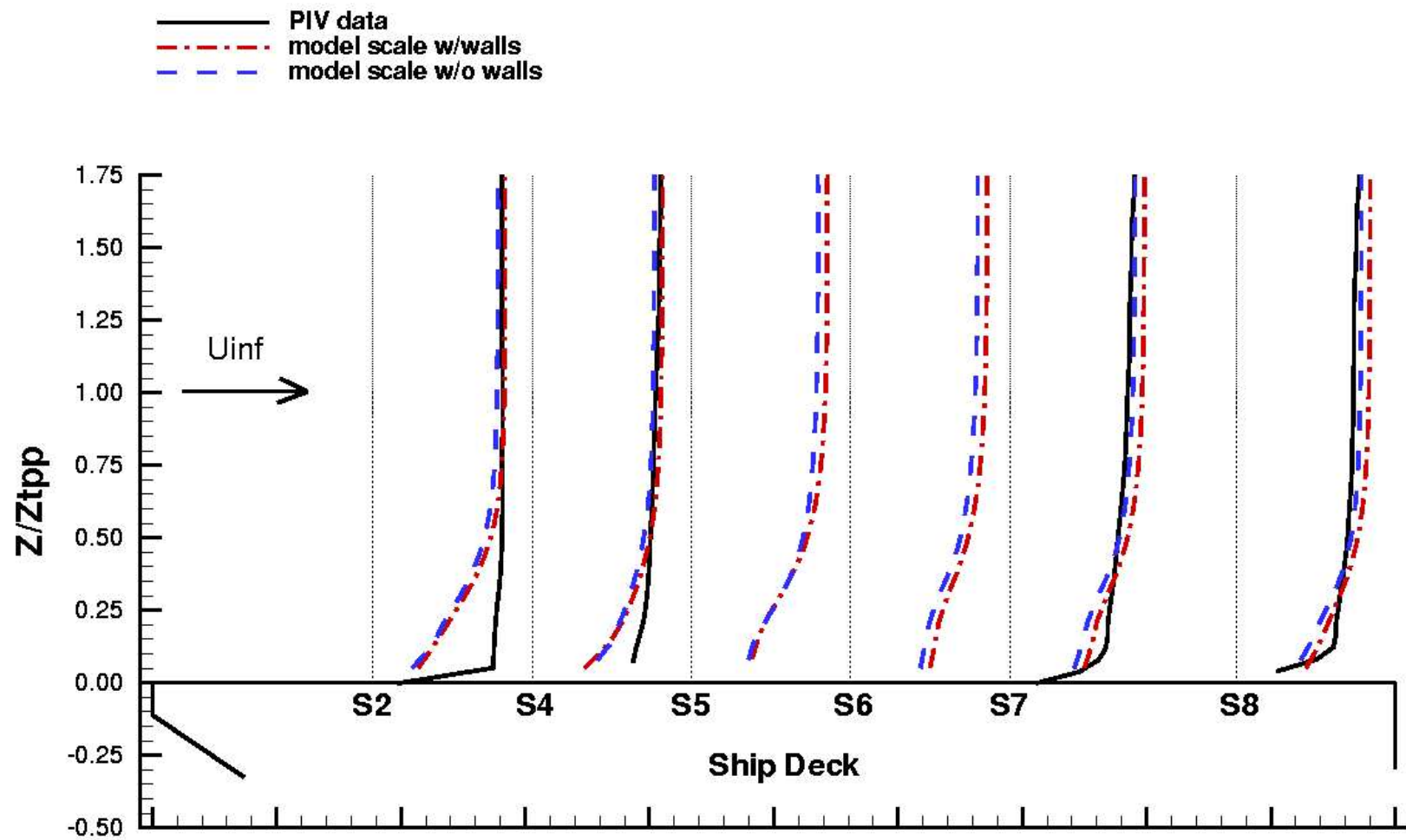
Figure 12. Comparison of measured and calculated deck boundary.
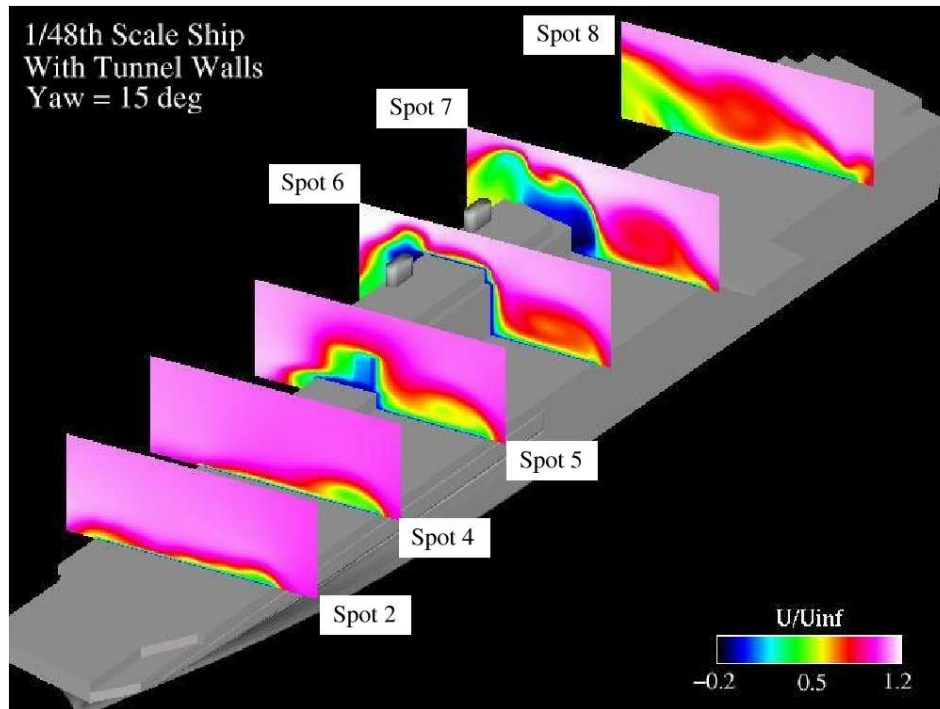
(a) Calculation (with walls)
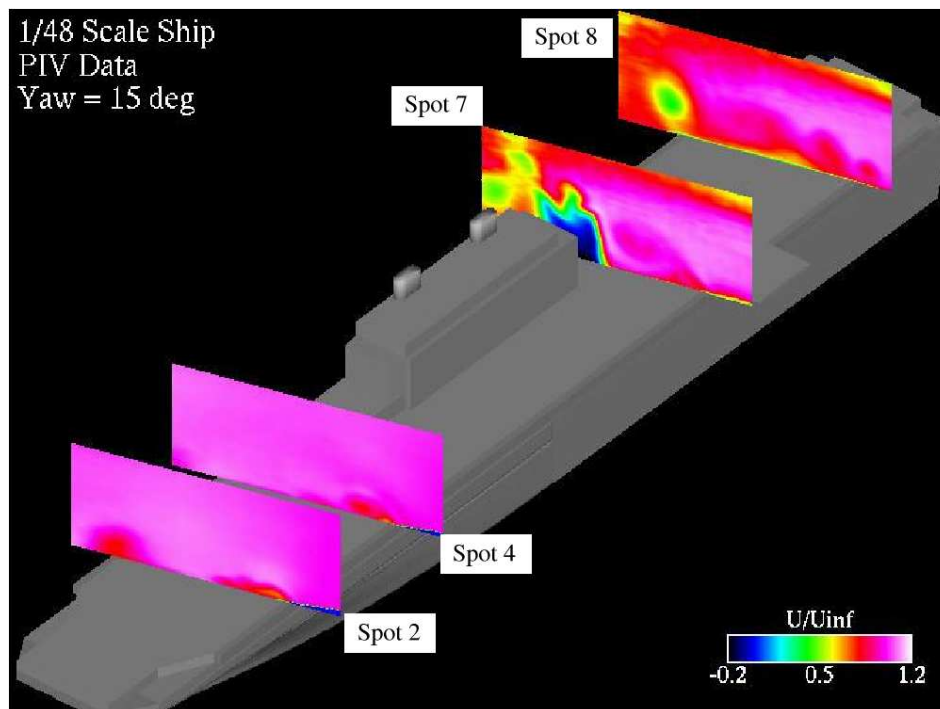
(b) PIV measurements

Figure 13. Comparison between calculated and measured ship airwake for yaw = 15 deg. Uinf = 22.5 ft/s.
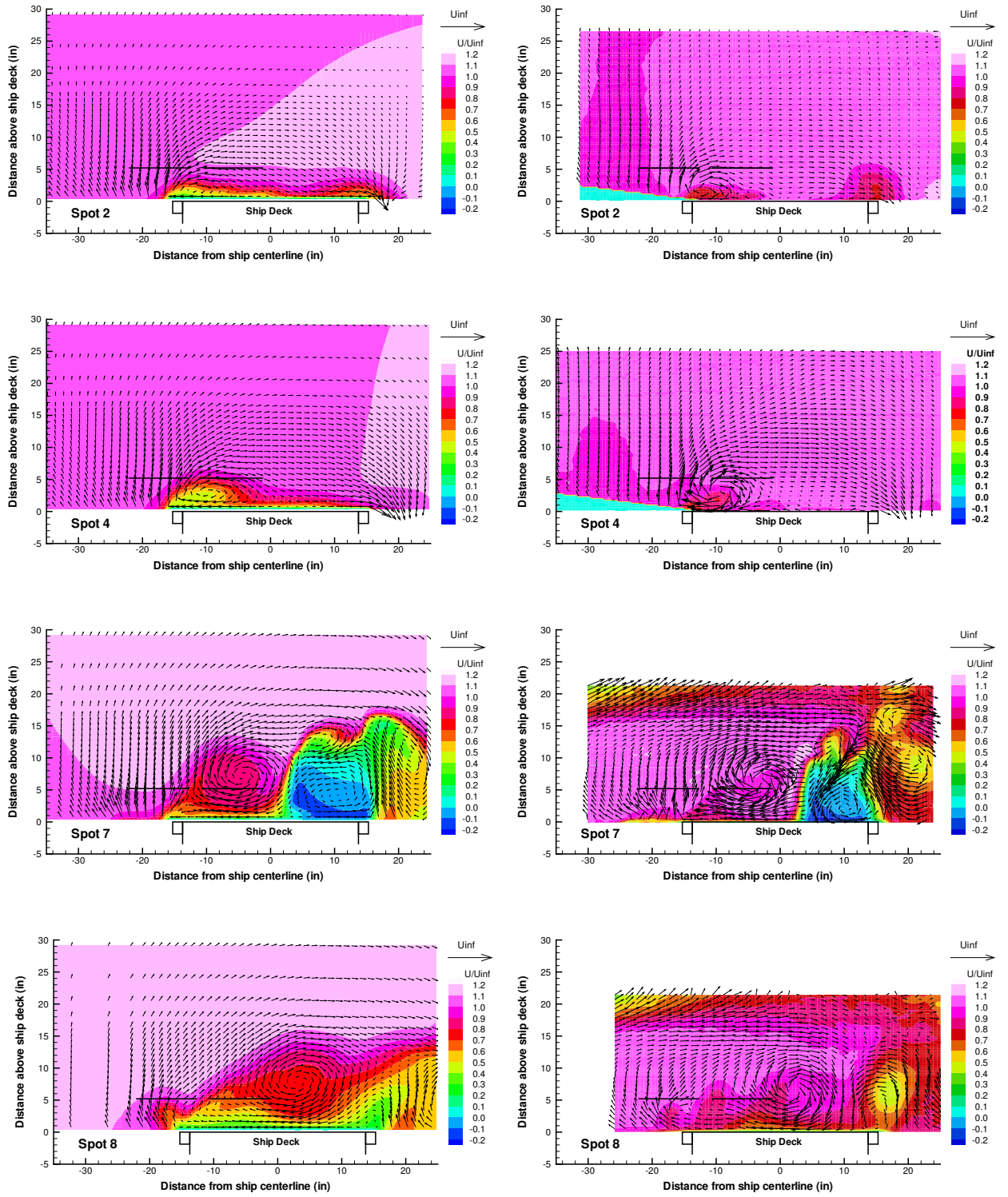
(a) Calculation (with walls)

(b) PIV measurements

Figure 14. Comparison between calculated and measured velocity fields for Landing Spots 2, 4, 7 and 8. Ship yaw = 15 deg. Unif = 22.5 ft/s. View looking upstream.
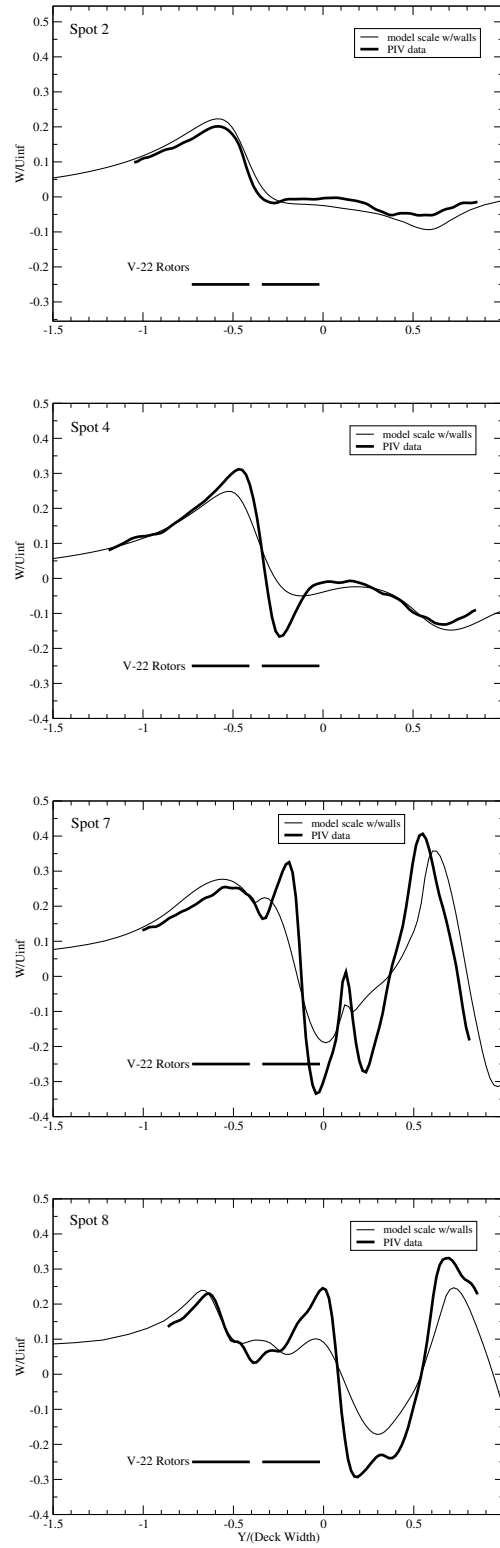
Figure 15. Comparison between calculated and measured vertical velocity across the ship deck at Landing Spots 2, 4, 7 and 8. Ship yaw = 15 deg. Uinf = 22.5 ft/s.
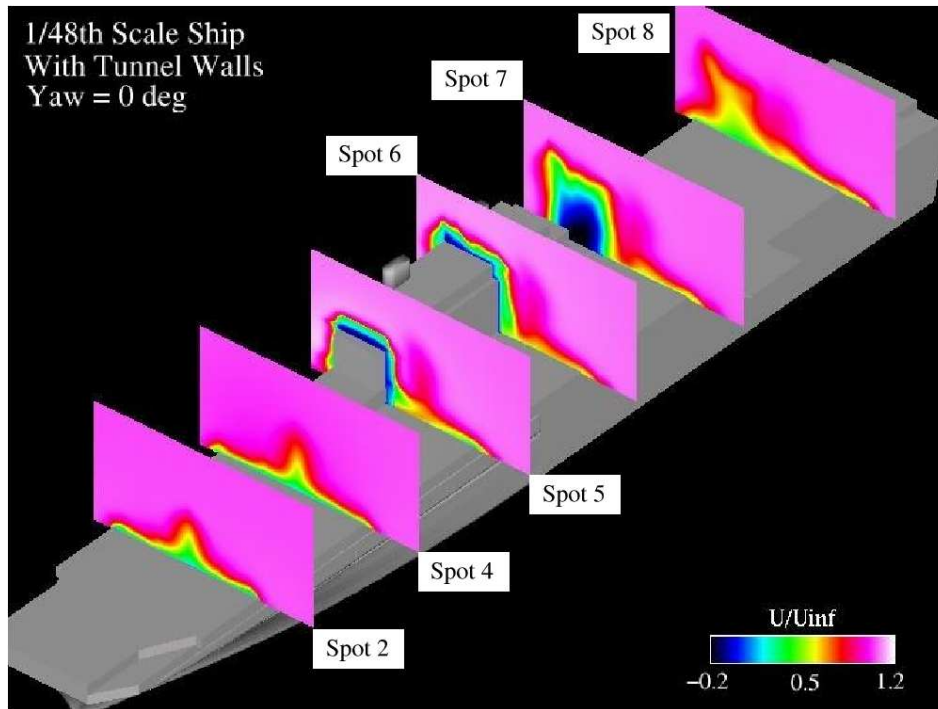
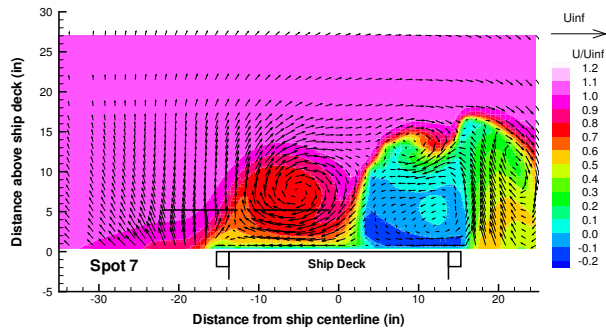(a) Calculation (with walls)
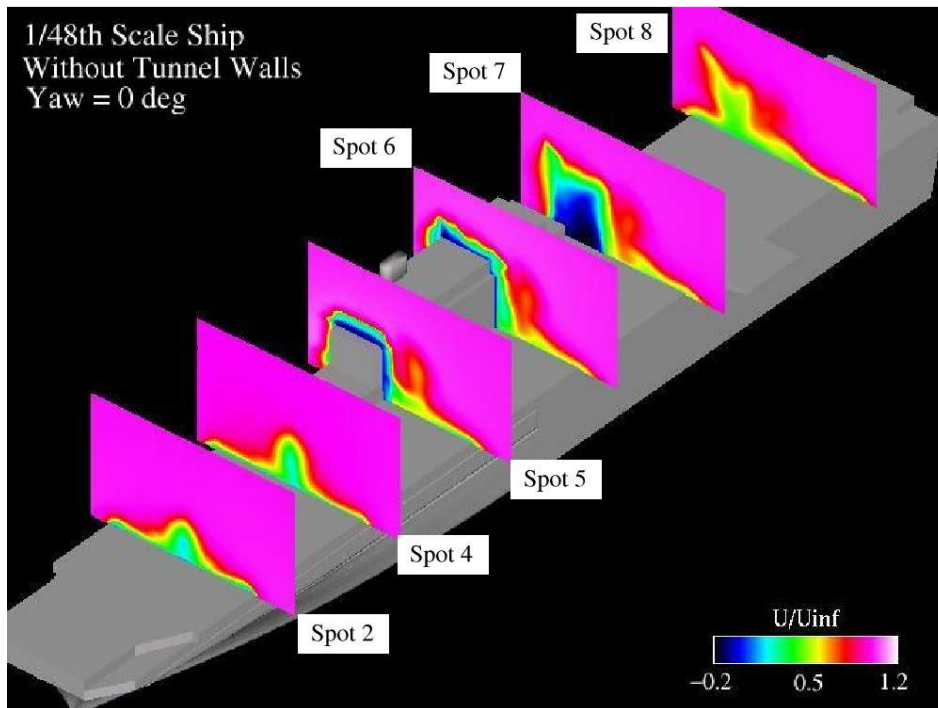
(b) Calculation (without walls)

Figure 16. Effect of wind tunnel walls on the calculated ship airwake. Ship yaw = 0 deg, Uinf = 22.5 ft/s.
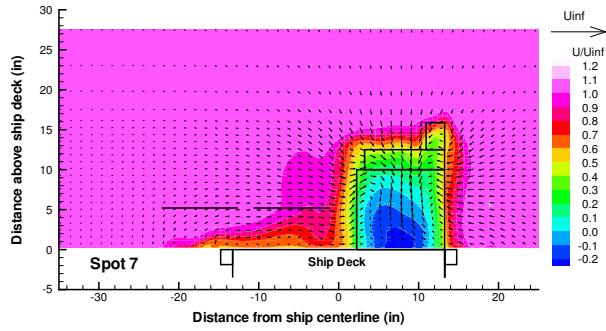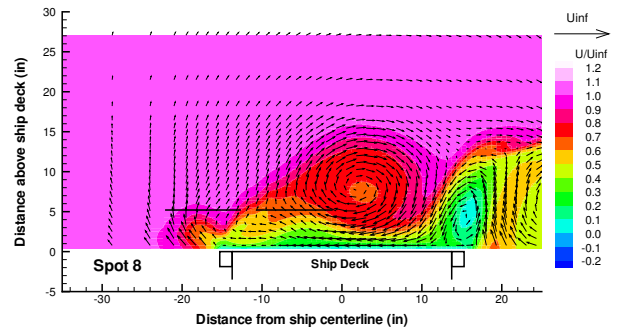
(a) Calculation (with walls)
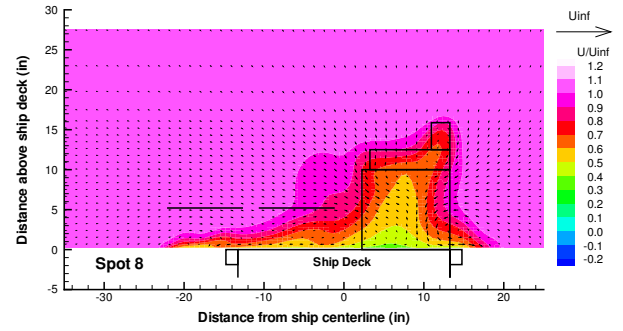

(a) Calculation (with walls)
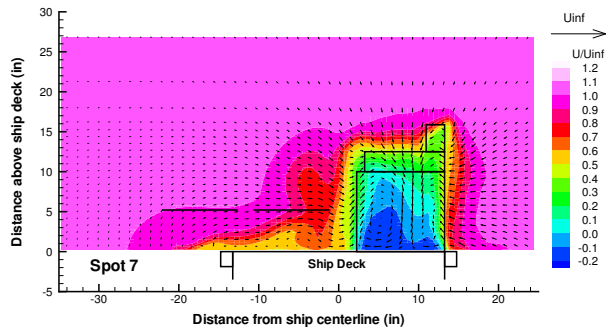
(b) Calculation (without walls)
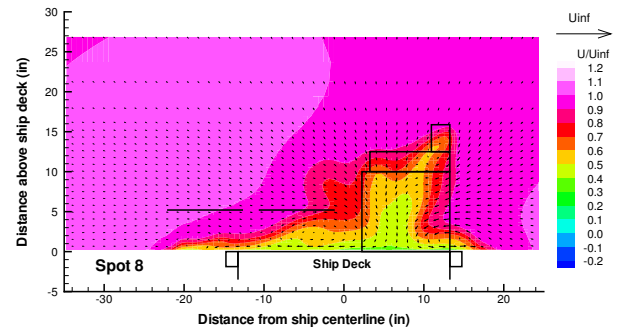
(b) Calculation (without walls)

Figure 17. Effect of wind tunnel walls on the calculated velocity field at Landing Spot 7. Ship yaw = 0 deg, Uinf = 22.5 ft/s. View looking upstream.
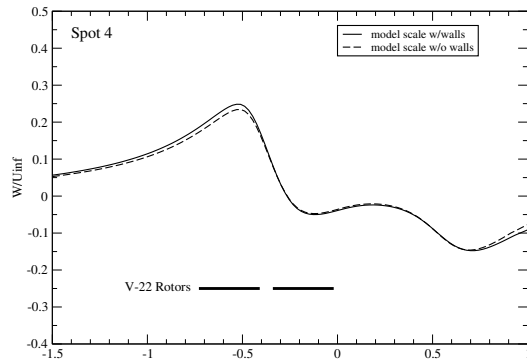
Figure 18. Effect of wind tunnel walls on the calculated velocity field at Landing Spot 8. Ship yaw = 0 deg, Uinf = 22.5 ft/s. View looking upstream.
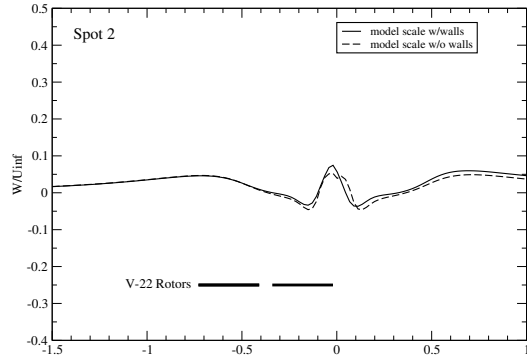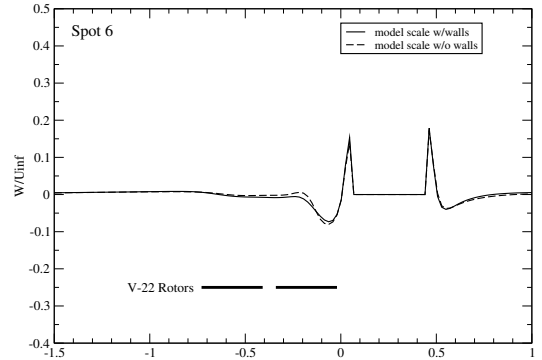
(a) Landing Spot 2
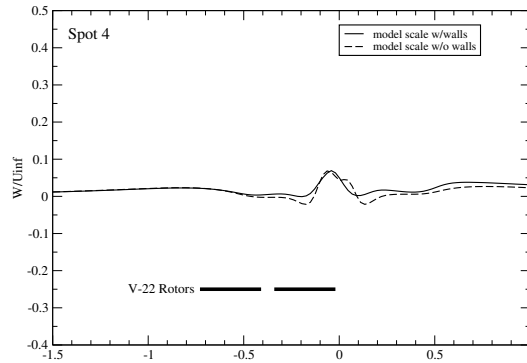
(b) Landing Spot 4
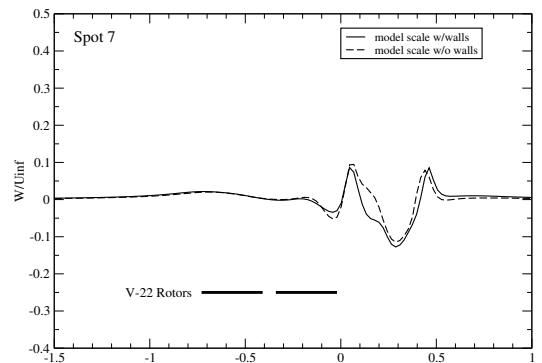
(c) Landing Spot 5
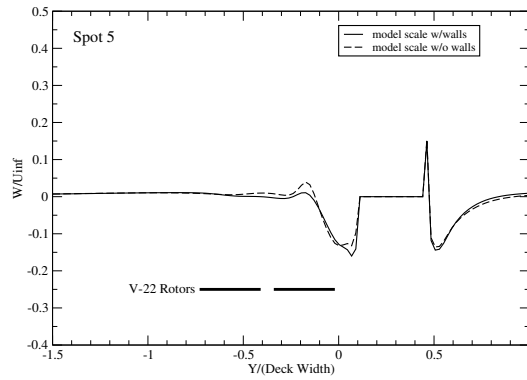
(d) Landing Spot 6
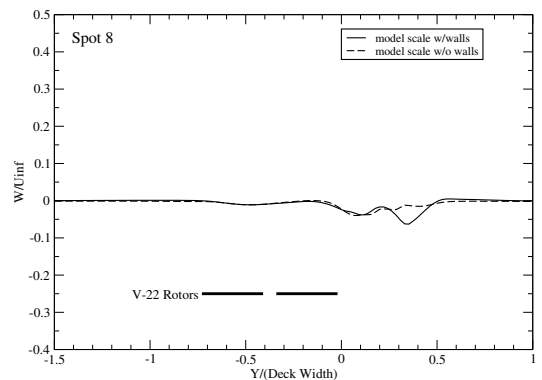
(e) Landing Spot 7

(f) Landing Spot 8

Figure 19. Effect of wind tunnel walls on the calculated vertical velocity across the ship deck. Ship yaw = 0 deg, Uinf = 22.5 ft/s.
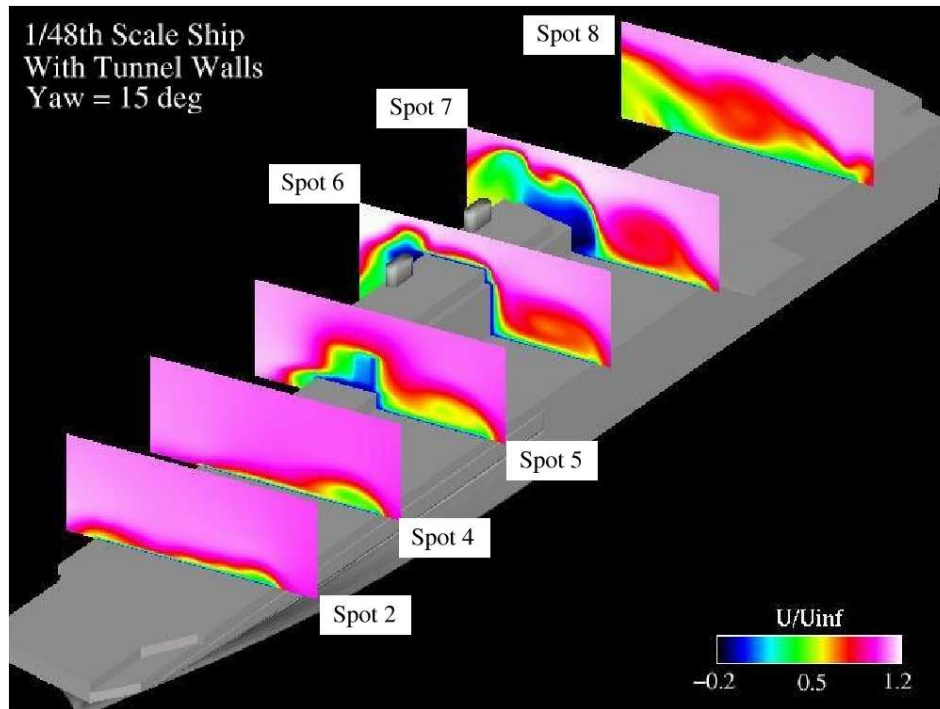
(a) Calculation (with walls)
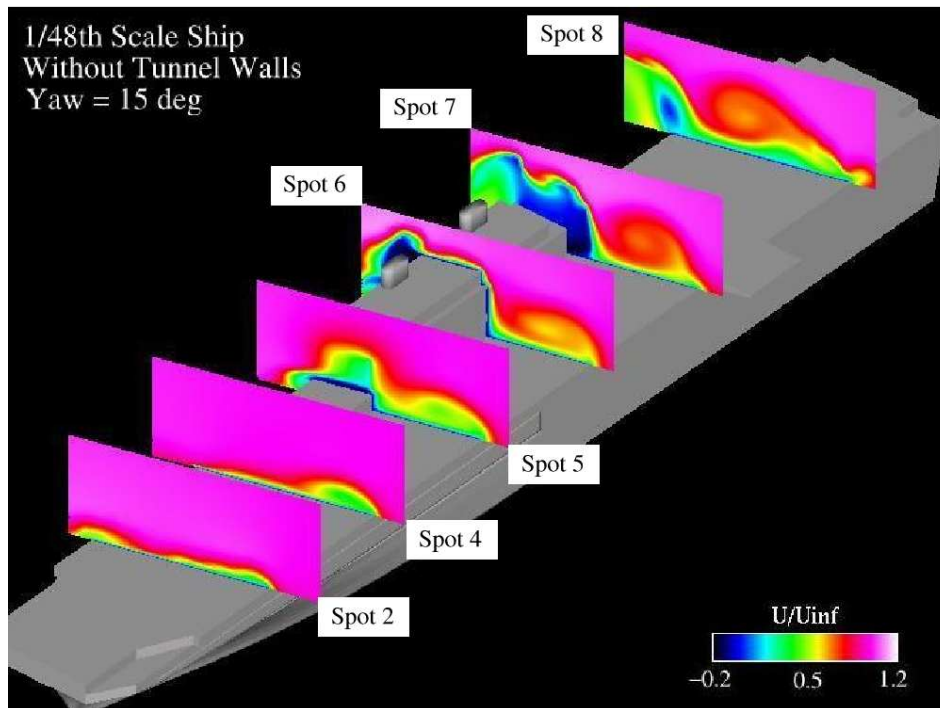
(b) Calculation (without walls)

Figure 20. Effect of wind tunnel walls on the calculated ship airwake. Ship yaw = 15 deg, Uinf = 22.5 ft/s.

(a) Calculation (with walls)

(b) Calculation (without walls)

Figure 21. Effect of wind tunnel walls on the calculated velocity field at Landing Spot 7. Ship yaw = 15 deg, Uinf = 22.5 ft/s. View looking upstream.
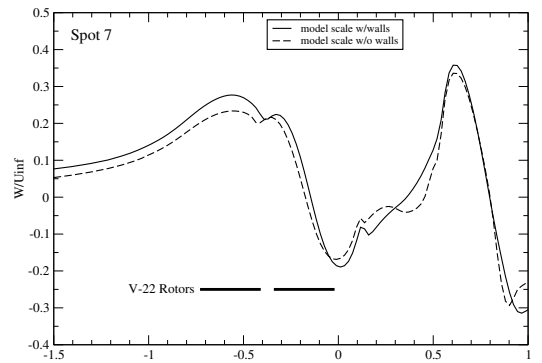

(a) Calculation (with walls)

(b) Calculation (without walls)

Figure 22. Effect of wind tunnel walls on the calculated velocity field at Landing Spot 8. Ship yaw = 15 deg, Uinf = 22.5 ft/s. View looking upstream.
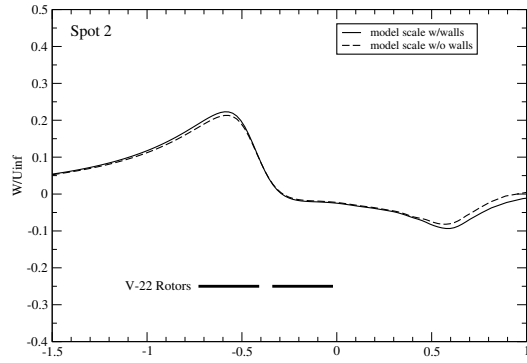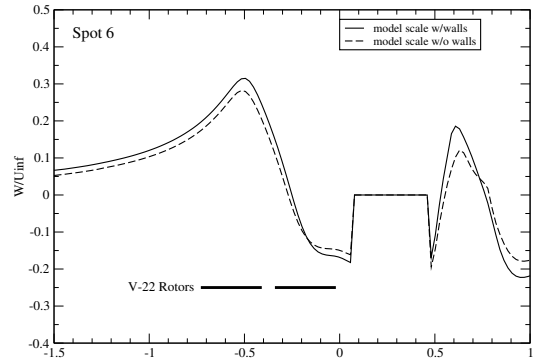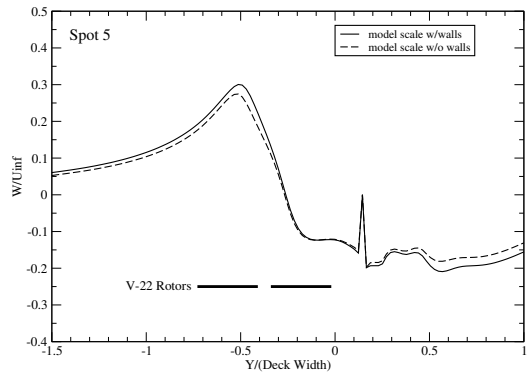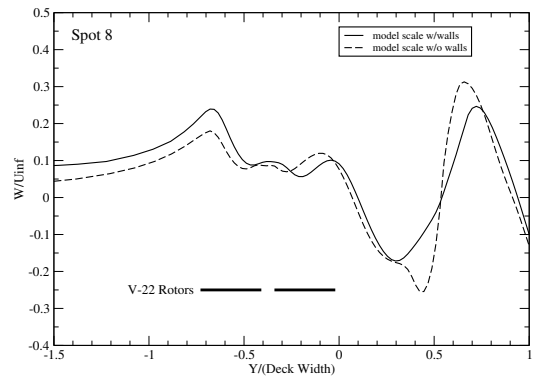
(a) Landing Spot 2

(b) Landing Spot 4

(c) Landing Spot 5

(d) Landing Spot 6

(e) Landing Spot 7

(f) Landing Spot 8

Figure 23. Effect of wind tunnel walls on the calculated vertical velocity across the ship deck. Ship yaw = 15 deg, Uinf = 22.5 ft/s.

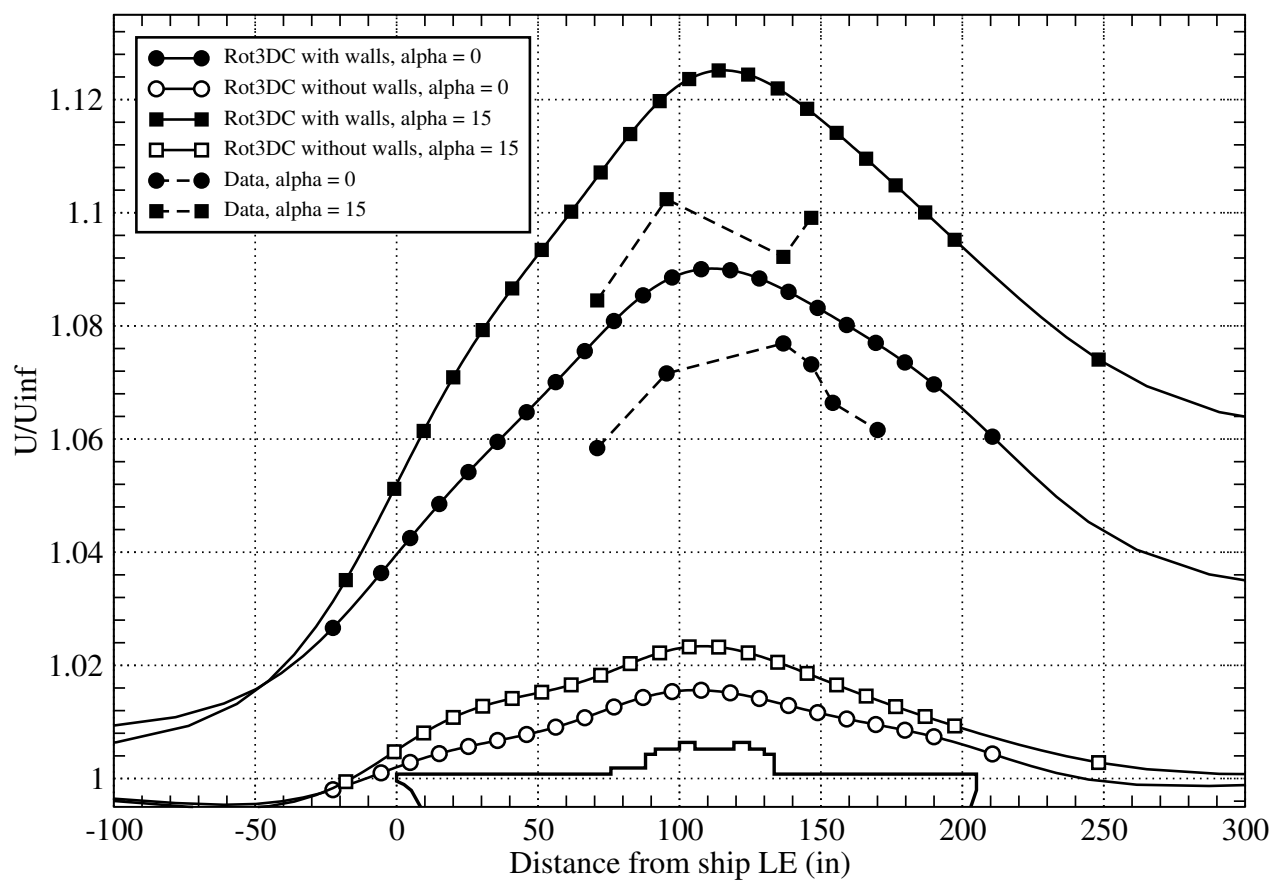Figure 24. Variation of calculated and measured streamwise velocity close to the test section ceiling. Uinf = 22.5 ft/s.